

CONFIDENTIAL

FEB 3 1953

NACA RM L52L30



NACA

RESEARCH MEMORANDUM

EFFECTS OF WING ELASTICITY ON THE AERODYNAMIC
CHARACTERISTICS OF AN AIRPLANE CONFIGURATION HAVING
45° SWEPTBACK WINGS AS OBTAINED FROM FREE-FLIGHT
ROCKET-MODEL TESTS AT TRANSONIC SPEEDS

By A. James Vitale

Langley Aeronautical Laboratory
Langley Field, Va.

CLASSIFIED DOCUMENT

This material contains information affecting the National Defense of the United States within the meaning of the espionage laws, Title 18, U.S.C., Secs. 793 and 794; the transmission or revelation of which in any manner to an unauthorized person is prohibited by law.

NATIONAL ADVISORY COMMITTEE
FOR AERONAUTICS

WASHINGTON

January 28, 1953

To

By authority of

Effective Date 4-8-57
NACA Res. Dir. 4 RN-114
NS 6-22-57

CLASSIFICATION CHANGED

UNCLASSIFIED

CONFIDENTIAL

NACA LIBRARY
LANGLEY AERONAUTICAL LABORATORY
Langley Field, Va.

NATIONAL ADVISORY COMMITTEE FOR AERONAUTICS

RESEARCH MEMORANDUM

EFFECTS OF WING ELASTICITY ON THE AERODYNAMIC
CHARACTERISTICS OF AN AIRPLANE CONFIGURATION HAVING
45° SWEEPBACK WINGS AS OBTAINED FROM FREE-FLIGHT
ROCKET-MODEL TESTS AT TRANSONIC SPEEDS

By A. James Vitale

SUMMARY

Flight tests at transonic speeds have been made of two rocket-propelled models of an airplane configuration having 45° sweptback wings of aspect ratio 4 and with different stiffnesses. The longitudinal stability, lift, and drag characteristics were determined by analysis of the response of the models to disturbances in pitch. A comparison was made between experimental and calculated effects of aeroelasticity on lift and longitudinal stability.

A straight-line extrapolation of the lift-curve slopes of the two wings of different stiffness to obtain the rigid-wing lift-curve slope was found to be satisfactory in the range of wing stiffness tested. The loss in lift-curve slope of the more flexible wing found experimentally agreed fairly well with that calculated by a modified strip-theory method. A combination of the effects of a high-tail position and an unstable pitching-moment curve of the wing at high lift coefficients and transonic speeds caused both models to execute a violent pitch-up maneuver. The induced drag parameter dC_D/dC_L^2 was found to be nonlinear with lift coefficient and the model having the more flexible wing had lower drag due to lift over the Mach number range of 0.97 to 1.30.

INTRODUCTION

The results presented in this paper are part of a general research program utilizing rocket-propelled models to investigate the effect of wing plan form on transonic and supersonic longitudinal stability, lift, and drag characteristics. Previous models tested have included several thin straight wings and triangular wings (refs. 1 to 6). All the models tested have had similar fuselage and tail surfaces. The wing-off characteristics of the models tested are presented in reference 2.

In this investigation two models were tested which had wings of different stiffnesses. The two wings differed in stiffness by reason of the material of construction, one having been constructed of solid steel and the other of solid duralumin. Since the only difference between the two models was wing stiffness, differences in the test results may be attributed to aeroelastic effects. The wings which had an aspect ratio of 4 and a taper ratio of 0.60 were swept back 45° at the quarter-chord line. The wing airfoil sections parallel to free stream were NACA 65A006.

An all-movable horizontal tail was used for longitudinal control on the models. During the flight the horizontal tail was deflected in an approximate square-wave program between the limits of 0.14° and -3.0° for the steel-wing model and -0.72° and -4.60° for the duralumin-wing model. The pulsed-control technique discussed in detailed form in reference 1 was used to obtain and analyze the data.

In addition to experimental results, the losses in lift and longitudinal stability due to aeroelastic deflection were calculated for the duralumin-wing model by the method outlined in the appendix of this report.

The models were flown at the Langley Pilotless Aircraft Research Station at Wallops Island, Va.

SYMBOLS

C_N	normal-force coefficient, $\frac{a_n}{g} \frac{W/S}{q}$
C_c	chord-force coefficient, $\frac{-a_l}{g} \frac{W/S}{q}$
C_L	lift coefficient, $C_N \cos \alpha - C_c \sin \alpha$
C_D	drag coefficient, $C_c \cos \alpha + C_N \sin \alpha$
C_m	pitching-moment coefficient
N_w	wing normal force, lb
C_{N_w} or C_{L_w}	wing lift coefficient, $\frac{N_w}{qS}$
a_n	normal acceleration as obtained from accelerometer, ft/sec/sec

a_z	longitudinal acceleration as obtained from accelerometer, ft/sec/sec
W	model weight, lb
g	acceleration of gravity, ft/sec/sec
p	free-stream static pressure, lb/sq ft
p_o	standard sea-level static pressure, 2116 lb/sq ft
q	dynamic pressure, $\frac{\gamma}{2} \rho M^2$
M	Mach number
R	Reynolds number, based on wing mean aerodynamic chord
S	wing area, including the area enclosed within the fuselage, sq ft
\bar{c}	wing mean aerodynamic chord, ft
c	wing chord, ft
$b/2$	wing semispan, ft
y	lateral distance from fuselage center line, ft
y'	lateral distance from fuselage side, ft
L	load applied, lb
θ	local wing twist angle produced by L , radians; also angle of pitch, radians
$(\theta/L)_{ref}$	structural influence coefficient at spanwise center of pressure
α	angle of attack, deg
δ	horizontal-tail deflection, deg
γ	flight-path angle, deg
A	aspect ratio
P	period of oscillations, sec

$T_{1/2}$ time to damp to one-half amplitude, sec

l distance from center of gravity to nose normal accelerometer, ft

Subscripts:

$$\dot{\alpha} = \frac{1}{57.3} \frac{d\alpha}{dt} \frac{\bar{c}}{2V}$$

$$q = \frac{d\theta}{dt} \frac{\bar{c}}{2V}$$

w wing

e elastic

r rigid

cp center of pressure

MODELS AND APPARATUS

Models

A three-view drawing of the models used in this investigation is shown in figure 1. Photographs of the models are given in figure 2. The fuselage has a cylindrical center section with identical ogival type of nose and tail sections defined by the ordinates given in table I. The body fineness ratio is 13.0.

The two models tested had identical wings except for material of construction. One model had a wing constructed of solid steel, and the other model had a wing constructed of solid duralumin. The wing airfoil sections parallel to free stream were NACA 65A006 airfoil sections.

The horizontal tail was constructed of solid duralumin for both models and was mounted on a ball bearing built into the vertical tail at a height of 0.508 semispan above the wing-chord plane extended. A hydraulic power system was used to deflect the horizontal tail in an approximate square-wave program. The gap between the vertical tail and the root of the horizontal tail was sealed by means of a wiper-type seal.

The mass characteristics of the two models tested are given in the following table:

	Steel-wing model	Dural-wing model
W	146 pounds	119 pounds
I _y	10.30 slug-ft ²	10.95 slug-ft ²
c.g. position	24.8 percent MAC	4.6 percent MAC

Instrumentation

The models were equipped with telemeters transmitting measurements of normal acceleration at the model center of gravity, angle of attack, longitudinal acceleration, wing normal force, control position, total pressure, reference static pressure, and transverse acceleration. The duralumin-wing model had a normal accelerometer located 2.68 feet ahead of the model center of gravity in addition to the center-of-gravity normal accelerometer. This arrangement permitted the determination of instantaneous pitching moment for the duralumin-wing model.

A vane-type instrument mounted on a sting extending from the nose of the model (fig. 2) was used to measure angle of attack. For the duralumin-wing model this sting was deflected downward 5° to permit positive angle-of-attack measurements up to 20°. The angle-of-attack indicator is described in more detail in reference 7.

The wing was mounted on a beam-type balance calibrated to give measurements of wing normal force. The balance is described in more detail in reference 3. In addition to the inductance-gage pickup described in reference 3, the balance for the duralumin-wing model was equipped with a strain-gage pickup for development purposes.

The total-pressure pickup was mounted on a small strut below the fuselage. The static-pressure orifice was located 4.9 inches behind the beginning of the cylindrical portion of the fuselage. A calibration of the reference static pressure for an angle of attack of 0° was obtained from previous instrumentation models.

Atmospheric conditions were determined from radiosondes released shortly after the flights. Fixed and manually operated 16-millimeter motion-picture cameras were used to photograph the launchings and first portions of the flights. Additional ground equipment consisted of a CW Doppler radar unit for obtaining model velocity, a tracking radar unit for obtaining model position in space, and special (spinsonde) radio equipment for obtaining model rolling velocity.

TESTS

Preflight Measurements

Prior to flight testing the structural influence coefficients were obtained for the duralumin wing. These coefficients are shown in figure 3 as the twist in the free-stream direction per unit load applied along the 25- and 50-percent chord lines.

With instruments installed, the models were suspended by shock cords and vibrated in the pitch plane by an electromagnetic shaker and also by striking the wing and fuselage. The following model natural frequencies and modes of vibration were determined from the telemeter records taken during these ground tests and from visual observations of the model vibrating.

Wing mode	Frequency, cps	
	Steel wing	Duralumin wing
First bending	44	46
Second bending	212	206
Torsion	340	350

Model Tests

The models were launched at approximately 60° from the horizontal by means of a mobile launcher shown in figure 4. A 6-inch-diameter solid-fuel ABL Deacon rocket motor was used to boost each model to maximum velocity. The models contained no sustaining rocket motors and experienced decelerating flight after separation from their boosters. During the decelerating portion of the flights, the models experienced short-period oscillations in angle of attack, normal acceleration, longitudinal acceleration, and wing normal force following each horizontal-tail deflection.

The measured angle of attack was corrected to the angle of attack at the model center of gravity by the method of reference 7. The wing normal-force measurements were corrected for inertia effects to give aerodynamic forces.

The Mach numbers and dynamic pressures were calculated from telemetered total pressure and free-stream static pressure obtained from the combination of radiosonde and tracking radar data. The velocity obtained from the CW Doppler radar unit furnished a check at peak velocity on the

Mach numbers obtained from the pressure data. For use in comparing the aeroelastic properties of the wings in the present investigation with other results the values of free-stream pressure obtained during the model flights divided by standard sea-level pressure are presented in figure 5 as a function of Mach number.

Reynolds numbers (based on wing mean aerodynamic chord for each model) obtained during the flights are shown in figure 6.

Analysis

Time histories of the model short-period oscillations in angle of attack, normal acceleration, longitudinal acceleration, and wing normal force were analyzed by the method of reference 1 to obtain the longitudinal stability, lift, and drag characteristics for each model.

In addition to obtaining longitudinal stability characteristics by the method of reference 1 the instantaneous pitching moment was measured for the duralumin-wing model by means of two normal accelerometers located at the center of gravity and in the nose of the model. The difference in the two normal-accelerometer readings is proportional to the angular acceleration in pitch by the relation:

$$\ddot{\theta} = \frac{a_{n_{\text{nose}}} - a_{n_{\text{cg}}}}{l}$$

The pitching moment due to angle of attack is then calculated by the following equation:

$$C_m(\alpha) = \frac{I_y \ddot{\theta}}{q S \bar{c}} - (C_{m\dot{\theta}} + C_{m\dot{\alpha}}) \dot{\alpha} - C_{m\dot{\theta}} \dot{\gamma}$$

For the steel-wing model, a nose accelerometer was not used but the instantaneous pitching moments were calculated from the flight data by use of a differentiation process. The angular acceleration in pitch was obtained from the following equation:

$$\ddot{\theta} = \frac{d\dot{\theta}}{dt} = \frac{d(\dot{\gamma} + \dot{\alpha})}{dt}$$

The quantity $\dot{\alpha}$ was obtained by differentiating the measured α curve and the quantity $\dot{\gamma}$ was calculated from the measured accelerations at the model center of gravity, the gravity component being neglected.

This procedure is the same procedure used in applying the corrections to the angle of attack measured at some point other than the center of gravity (ref. 7). Neglecting the gravity component has a negligible effect for these models.

The effects of aeroelastic distortion of the duralumin wing on lift and stability characteristics were calculated by means of a modified strip theory and the structural influence coefficients shown in figure 3. The method of calculating the aeroelastic effects is outlined in the appendix of this report.

Data were obtained for the steel-wing model from Mach numbers 0.97 to 1.27 and for the duralumin-wing model from Mach numbers 0.92 to 1.33. At a Mach number of 0.97 for the steel-wing model and 0.92 for the duralumin-wing model, the models experienced a pitch-up maneuver to high angles of attack and were not able to recover; thus further data could not be obtained.

Accuracy

The following tables give estimated values of the possible systematic errors in the absolute values of C_L , C_D , and C_{L_w} as affected by the accelerometer and wing-balance calibration ranges:

For the steel-wing model,

M	ΔC_L	ΔC_{L_w}	ΔC_D
0.97	± 0.020	± 0.016	± 0.004
1.15	± 0.013	± 0.010	± 0.003
1.30	± 0.009	± 0.008	± 0.002

and for the duralumin-wing model,

M	ΔC_L	ΔC_{L_w}	ΔC_D
0.92	± 0.015	± 0.011	± 0.004
1.15	± 0.009	± 0.006	± 0.0023
1.35	± 0.006	± 0.005	± 0.0016

Further errors in aerodynamic coefficients may arise because of possible dynamic-pressure inaccuracies which are approximately twice as great as the errors in Mach number. The Mach numbers are estimated to be accurate to ± 1 percent at supersonic speeds and ± 2 percent at subsonic speeds.

The exposed-wing lift data indicate a further error in the absolute value of the wing normal-force measurements for the duralumin-wing model. As stated in the instrumentation section, the wing balance for the duralumin-wing model was equipped with a strain-gage pickup for development purposes. The data from the strain-gage pickup do not indicate the zero-shift of about 200 pounds shown in figure 8 for the exposed duralumin-wing lift data from the inductance-gage pickup. This zero shift does not affect the incremental values or slopes which are, in general, more accurate than the absolute values.

The errors in the measured angles of attack and elevator deflections should not vary with Mach number because they are not dependent on dynamic pressure. The greatest possible error in angle of attack is caused by possible aerodynamic asymmetry of the angle-of-attack vane which is not detectable prior to flight. The following table gives estimated values for the errors in absolute values of α and δ as affected by instrument calibration ranges:

	$\Delta\alpha$	$\Delta\delta$
Steel-wing model	$\pm 0.17^\circ$	$\pm 0.1^\circ$
Duralumin-wing model	$\pm .25^\circ$	$\pm .1^\circ$

RESULTS AND DISCUSSION

Lift

The basic lift data are shown in figures 7 and 8 for the duralumin- and steel-wing models at several Mach numbers and horizontal tail deflections. In figure 7, the total lift coefficients are plotted against angle of attack for both models. It is seen from these curves that the lift-curve slope is nonlinear with lift coefficient. In figure 7(a) it is seen that the lift-curve slope near zero lift at Mach numbers 1.02 and 1.22 is about 15 percent lower than the lift-curve slope near lift coefficient of 0.30. At higher angles of attack as shown by the lift curves for Mach numbers 0.97, 1.12, and 1.27, the lift-curve slopes again decrease due to separation over the wing tips. Shown in figure 7(b)

is the lift curve for the duralumin-wing model at a Mach number of 0.92 and over an angle-of-attack range from 4° to 18° . The lift coefficient 0.70 at which the pitch-up occurred is well below the maximum lift coefficient obtainable at a Mach number of 0.92.

In figure 8 the exposed-wing lift coefficients are plotted against angle of attack for both models. The wing balance measures normal force only; however, the difference between normal force and lift force was estimated to be small for the exposed wing and the data are plotted as lift coefficients. The same nonlinear trends described in the previous section on total airplane lift are seen to apply also to the exposed-wing lift. This phenomenon of increase in slope at 0.20 to 0.40 lift coefficient and then decrease in slope at higher lift coefficients was also found in wind-tunnel tests on this wing (refs. 8 and 9).

The variation of lift-curve slope with Mach number is shown in figure 9 for the exposed wings and complete models. The slopes are taken near a lift coefficient of 0.30 since data were available at this lift coefficient for both horizontal-tail deflections. The duralumin-wing lift-curve slopes for the complete model and exposed wing increase rapidly from a Mach number of 0.92 to 0.95 and then gradually decrease as the Mach number increases. The steel-wing lift-curve slopes show the same variation with Mach number but, as would be expected, have higher values than for the more flexible duralumin wing. Also shown in figure 9 is the lift-curve slope of the exposed rigid wing as obtained by the method described in the section entitled "Aeroelastic Effects on Lift."

The ratio of the exposed-wing lift to complete-model lift is shown in figure 10. The values were obtained by dividing the exposed-wing lift-curve slopes by the complete-model lift-curve slopes shown in figure 9 for a lift coefficient of 0.30. The contribution of the wing to the complete-model lift is approximately constant over the Mach number range covered for both models. The ratio of exposed-wing area to total wing area is 0.78 for the models tested. For the steel-wing model the ratio of exposed-wing lift to total lift varies from 0.75 at a Mach number of 1.0 to 0.71 at a Mach number of 1.27. When the tail contribution to the total lift is taken into account the results for the steel wing show that the usual assumption that the fuselage carries that part of the load represented by the wing area intercepted by the fuselage gives nearly correct answers over the Mach number range 0.97 to 1.27. The exposed duralumin wing carried a slightly smaller percentage of the total lift than the exposed steel wing from Mach numbers 1.0 to 1.30.

Model Vibrations

For the duralumin-wing model there was a high-frequency oscillation of 180 cycles per second superimposed on the telemetered traces of angle of attack and nose normal acceleration from Mach numbers 1.46 to 1.25. This type of nose vibration which started near the time of booster-rocket burnout also occurred on a similar model having a considerably different wing tested in reference 6.

Near the beginning of the pitch-up maneuver of the steel-wing model (discussed in the static stability section) at a Mach number of 0.965 and lift coefficient of 0.64 the wing normal-force and normal-acceleration measurements indicated a vibration corresponding to the wing first-bending frequency which was probably caused by wing buffeting. A similar vibration occurred at the beginning of the pitch-up maneuver of the duralumin-wing model at a Mach number of 0.92 and lift coefficient of 0.70. At a Mach number of 0.955 and lift coefficient of 0.56, there also was an indication of wing buffeting for the duralumin-wing model.

Aeroelastic Effects on Lift

For use in calculating the loss in lift of the duralumin wing, the structural influence coefficients were measured before the model was tested. These influence coefficients are shown in figure 3 for concentrated loads along the 0.25 chord line and the 0.50 chord line. It was assumed that structural influence coefficients of the steel wing were related to the values measured for the duralumin wing by the ratio of the modulus of elasticity of duralumin to that of steel. One method of using these structural influence coefficients is shown in figure 11. Data obtained from reference 10 at a Mach number of 1.11 for a rocket model equipped with the same wing constructed of wood with duralumin inlays is compared with the complete-model lift-curve slopes of the steel and duralumin-wing models. The abscissa of figure 11 is the parameter $qS(\theta/L)_{ref}$ where $(\theta/L)_{ref}$ is the structural influence coefficient from figure 3 at the spanwise center of pressure of the exposed rigid wing for the load also applied at this spanwise location. Since the exposed-wing lift-curve slope was not measured in the test of reference 10 for the wood-duralumin wing and the ratio of tail area to wing area is nearly the same as for the steel- and duralumin-wing models, the complete-model lift-curve slopes are plotted against the parameter $qS(\theta/L)_{ref}$. When influence coefficients for both the 0.25-chord loading and the 0.50-chord loading are used, figure 11 shows that a straight-line extrapolation is possible over the range of stiffnesses for the three wings tested to obtain the value of the rigid lift-curve slope. The same method was used in figure 12 to obtain the rigid exposed-wing lift-curve slope at several Mach numbers. The variation of the rigid exposed-wing lift-curve slope with Mach number is shown in figure 9.

The loss in lift of the duralumin wing was calculated by means of the modified-strip-theory method outlined in the appendix. The method used allows the exposed wing to be divided into any number of sections and also allows any desired type of span loading to be used. Shown in figure 13 is the ratio of the elastic- to rigid-exposed-wing lift-curve slope of the duralumin wing calculated for two-point and five-point span loadings from a span-loading curve of reference 11. Since the exact location of the chordwise center of pressure was not known, the calculations were made by using the influence coefficients for both the 0.25-chord loading and the 0.50-chord loading. Pressure measurements on a similar wing tested in reference 12 show that these two positions should bracket the chordwise center-of-pressure variation along the span and that for this wing the 0.50-chord loading is more correct over the Mach number range 1.0 to 1.30. The results of figure 13 show that, for the wing tested, there is little difference in the ratio of the elastic to rigid lift-curve slope calculated by a two-point loading and by a five-point loading. The results from a calculation using a two-point loading from a trapezoidal span-load curve indicated only a 1-percent greater lift loss than a two-point solution using a span-load curve of reference 11.

The effect of wing-inertia loading which acts in the opposite direction to aerodynamic loading was included in the lift-loss calculations shown in figure 14. These calculations were made using equation 7 of the appendix for a two-point loading which includes the wing-inertia effect. The weight of one panel of the exposed duralumin wing was 5.93 pounds and the effect of including wing inertia in a two-point solution reduced the calculated lift loss by about 2 percent in the Mach number range 0.97 to 1.27 where the elastic-exposed-wing lift-curve slope varies from 90 to 80 percent of the rigid value.

A comparison between the calculated values and experimental values of the ratio of the exposed-duralumin-wing and exposed-rigid-wing lift-curve slopes of figure 9 is also shown in figure 14. At a Mach number of 0.97 the experimental ratio agrees with the calculated value for a 0.25-chord loading, and over the Mach number range 1.02 to 1.27 the experimental ratios agree with the calculated values for a 0.50-chord loading.

The loss in lift for the duralumin wing was also calculated from the charts of reference 13 at subsonic speeds and the values obtained agree fairly well with the calculations made by the method of the appendix at these same speeds. The charts were not used for higher speeds since reference 13 states that the charts are less reliable when the component of Mach number perpendicular to the leading edge of the wing is transonic.

The wind-tunnel investigation of reference 14 for a wing-fuselage combination having steel and duralumin wings similar to those of this report showed less reduction in lift for the duralumin-wing-fuselage combination than shown in figure 14 for the exposed duralumin wing of this investigation. The dynamic pressures for the investigation of reference 14, however, varied from only 400 to 850 pounds per square foot as compared with 1100 to 2500 pounds per square foot for the rocket-model investigation.

Static Stability

The basic pitching-moment data are shown in figure 15 for the steel-wing model at a center-of-gravity position of 24.8 percent of the mean aerodynamic chord, and in figure 16 for the duralumin-wing model at a center-of-gravity position of 4.60 percent of the mean aerodynamic chord. The pitching-moment coefficients are plotted against lift coefficient over the first one and one-half cycles of the model short-period oscillation following each horizontal-tail deflection. The measured pitching moments have been corrected for the damping-in-pitch derivatives, and the data of figures 15 and 16 do not show any consistent difference for increasing and decreasing angle of attack. As might be expected, the data obtained by using the double differentiation procedure show more scatter than those obtained from the double accelerometer method. The pitching-moment data at a Mach number of 0.97 and horizontal-tail deflection of -4.60° in figure 16 include the effect of a trim change at this Mach number. The change in trim lift coefficient is from 0.46 at a Mach number of 0.975 to 0.52 at a Mach number of 0.965.

At a Mach number of 0.97 the steel-wing model experienced a pitch-up maneuver to high angles of attack which was so violent that the model was not able to recover. At the peak of the maneuver the model developed a high rate of roll of about 15 radians per second; this high rate indicated that one wing stalled before the other wing. The pitching-moment curve (fig. 15) for this part of the flight could not be calculated above a lift coefficient of 0.82 because the angle-of-attack vane hit a stop at about 12° , although the model continued to pitch up to considerably higher angles. This pitch-up corresponds to the unstable break in the pitching-moment curve for this wing alone at high lift coefficients and transonic speeds. With the tail placed in the high position of 0.508 semispan above the wing-chord plane extended, the tail contribution to the longitudinal stability was not sufficient to overcome the unstable pitching-moment-curve slope of the wing at high lift coefficients. Further discussion of the effect of high tail position is found in reference 15.

The duralumin-wing model was tested with a center-of-gravity position approximately 20 percent of the mean aerodynamic chord more forward

than the steel-wing model. The pitching-moment data of figure 16 indicate that, at a Mach number of 0.97 and lift coefficient of 0.73, the duralumin-wing model approached the unstable break in the curve but did not overshoot into the unstable region. At a Mach number of 0.92, however, the duralumin-wing model experienced the same pitch-up maneuver described previously for the steel-wing model. The pitching-moment curve for this maneuver (fig. 16(a)) has a very unstable break at a lift coefficient of 0.70 and then indicates stable slope at 0.85 lift coefficient. The pitching-moment curve for the duralumin-wing model at a Mach number of 0.97 was converted to the center-of-gravity position for the steel-wing model and is shown by a dashed line in figure 15(a) for comparison with the data on the steel-wing model at the same Mach number. The curves are similar in shape and the displacement of the curves from each other is accounted for by the difference in horizontal-tail deflection.

The measured periods of oscillation of the angle of attack are shown in figure 17. The data shown for the duralumin-wing model are for a center-of-gravity position of 4.6 percent of the mean aerodynamic chord, and for the steel-wing model at 24.8 percent of the mean aerodynamic chord. The periods of oscillation were converted to the longitudinal stability derivative $C_{m\alpha}$ by the method described in reference 1. Since the two models were tested with different center-of-gravity positions, the static stability is compared in figure 18 on the basis of aerodynamic-center position. The duralumin-wing model shows a rapid rearward movement in aerodynamic center from 45 percent of the mean aerodynamic chord at a Mach number of 0.93 to 60 percent at a Mach number of 0.97. From a Mach number of 0.97 to 1.33 the aerodynamic center gradually moved rearward from 60 percent to 72 percent of the mean aerodynamic chord. Aerodynamic-center positions obtained from the pitching-moment data of figures 15 and 16 near trim conditions for the two models agree very well with the values calculated from the period of oscillations except for one point representing a curve obtained from the double differentiation procedure.

The aerodynamic-center position for the steel-wing model has the same variation with Mach number as the duralumin-wing model over the Mach number range 1.02 to 1.27. Over this Mach number range, however, the aerodynamic-center position is 3 to 6 percent more rearward for the steel-wing model. From the strip-theory method of the appendix the forward movement in aerodynamic-center position due to the inboard movement of the span load was calculated for the duralumin-wing model. A comparison between the calculation made for a 0.50-chord loading and the measured difference in aerodynamic-center position for the steel- and duralumin-wing models in figure 18 shows that nearly all of the loss in stability of the duralumin-wing model may be accounted for by the inboard movement of load on the wing.

Damping in Pitch

The time required for the pitch oscillations to damp to one-half amplitude is shown in figure 19(a) for the steel-wing model and in figure 19(b) for the duralumin-wing model. The data converted to the damping-in-pitch derivative $C_{m\dot{q}} + C_{m\dot{\alpha}}$ are shown in figure 19(c). The duralumin-wing-model data of figure 19 are presented for a center-of-gravity position 20 percent of the mean aerodynamic chord more forward than for the steel-wing model. The difference in center-of-gravity position was calculated to have a small effect on the damping-in-pitch derivatives of figure 19(c). Also shown in figure 19(c) is the damping-in-pitch derivative from the wing-off model of reference 2 converted to the dimensions and average center-of-gravity position of the steel- and duralumin-wing models.

The pitch-damping derivative for the duralumin-wing model shows a rapid variation with Mach number in the transonic speed range. This same variation would probably have occurred for the steel-wing model also, but damping data were not obtained for the steel-wing model below a Mach number of 1.0. The lower value of $C_{m\dot{q}} + C_{m\dot{\alpha}}$ for the duralumin-wing model from Mach numbers 1.02 to 1.2 may not be due to aeroelasticity and is more likely an indication of the accuracy of the damping-in-pitch derivative. Since the damping derivative for the wing-off model is essentially $C_{m\dot{q}}$ of the tail, the data of figure 19(c) show that the wing contribution to the damping derivative $C_{m\dot{q}} + C_{m\dot{\alpha}}$ is very small over the Mach number range 1.15 to 1.30.

Drag

The basic drag data for the steel- and duralumin-wing models is shown in figures 20 and 21 for several Mach numbers and horizontal-tail deflections. The drag data for the duralumin-wing model shown in figure 21(c) for an average Mach number of 0.97 were plotted over the Mach number range 0.965 to 0.975 and show that because of the transonic drag rise there is a noticeable change in the level of the drag polars with a small change in speed.

The minimum drag values obtained for both models are compared with the minimum drag of the wing-off model of reference 2 in figure 22. Also shown in figure 22 is the wing-plus-interference drag obtained from the large-scale drag test of reference 16. The wing-plus-interference drag obtained from the steel- and duralumin-wing-model tests compares favorably with the values of reference 16 at supersonic speeds. Because of the small size of the wing relative to the body and the high-drag body and tail, the wing drag represents a small percentage of the drag of the

steel- and duralumin-wing models. Thus, at a Mach number of 0.94, the wing drag is about the same magnitude as the accuracy of the accelerometer readings of the steel- and duralumin-wing models.

The drag due to lift of the models tested is presented in figure 23(a) for lift coefficients of 0.50 and in figure 23(b) for lift coefficients of 0.15 since the induced drag was found to be nonlinear with lift coefficient. Also shown in figure 23 is the ideal induced-drag factor $1/\pi A$ and the drag due to lift for no leading-edge suction $1/57.3C_{L\alpha}$. For the $1/57.3C_{L\alpha}$ comparison, the lift-curve slopes were measured near the trim-lift coefficient corresponding to elevator deflections of -3.0° and 0.14° for the steel-wing model and -4.60° and -0.72° for the duralumin-wing model.

Near lift coefficients of 0.50 the duralumin-wing model shows a reduction in induced drag of about 16 percent compared to $1/57.3C_{L\alpha}$ over the Mach number range 0.92 to 1.33. The data for the steel-wing model show no reduction in induced drag from Mach numbers of 1.05 to 1.27 for lift coefficients of 0.50.

At low lift coefficients near 0.15, the duralumin-wing model shows a reduction in dC_D/dC_L^2 of about 30 percent from Mach numbers 1.02 to 1.25 and 42 percent at a Mach number of 0.93 compared to the factor $1/57.3C_{L\alpha}$. The steel-wing model shows a reduction of 18 percent in dC_D/dC_L^2 at low lift coefficients over the Mach number range 1.02 to 1.22. The wind-tunnel investigation of reference 14 for lower dynamic pressures than the present investigation indicates only slightly lower drag for the duralumin-wing-fuselage combination than for the steel-wing-fuselage combination.

The lower induced drag for the duralumin-wing model suggests the possibility of a more efficient span loading for the flexible wing as a result of the inboard movement of the load when the wing deflects.

CONCLUSIONS

The flight tests of two rocket-propelled models having 45° swept-back wings of aspect ratio 4 and with different stiffnesses indicated the following results:

1. The loss in lift-curve slope due to aeroelastic distortion found experimentally agrees very well with that predicted by a modified-strip-theory method of calculation.

2. In the stiffness range investigated, a straight-line extrapolation of the lift-curve slopes of wings with different stiffnesses can be used to obtain the value for a rigid wing.

3. The exposed duralumin wing carried a slightly smaller percentage of the total airplane lift than the exposed steel wing from Mach numbers 1.0 to 1.30.

4. Because of the combined effects of an unstable break in the pitching-moment curve of the wing and a high tail position, the two airplane configurations tested experienced violent pitch-up maneuvers at transonic speeds and lift coefficients below the maximum.

5. The more forward aerodynamic-center position for the airplane configuration having a duralumin wing was mostly due to the inboard movement of the spanwise center of pressure.

6. Over the Mach number range 1.15 to 1.30, the wings tested contributed very little to the damping-in-pitch derivative $C_{mq} + C_{m\dot{\alpha}}$.

7. The induced-drag parameter dC_D/dC_L^2 was nonlinear with lift coefficient such that both models tested had higher values of dC_D/dC_L^2 at a lift coefficient of 0.50 than at a lift coefficient of 0.15.

8. The airplane configuration having a duralumin wing had lower drag due to lift than the steel-wing model; this fact suggests the possibility of a more efficient span loading for the more flexible wing.

Langley Aeronautical Laboratory,
National Advisory Committee for Aeronautics,
Langley Field, Va.

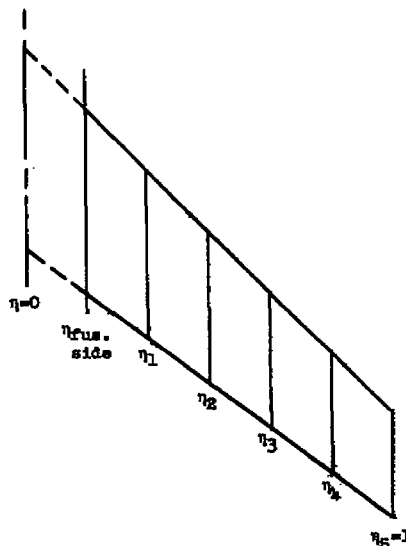
APPENDIX

EFFECTS OF AEROELASTIC DEFLECTION

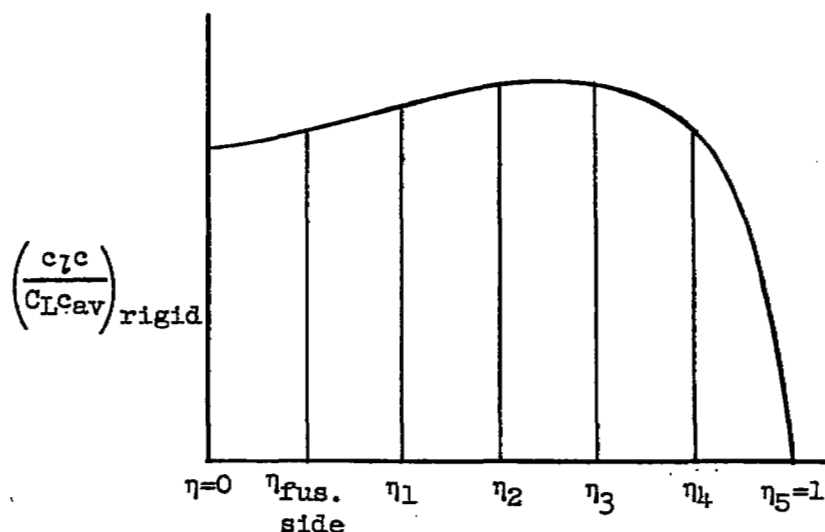
The method used to estimate the change in lift and center of pressure due to elastic deflection of the wing is a form of strip theory. The information needed to apply this method is data on twist along the wing due to unit loads applied along the centers of pressure (taken to be along the 0.25 or 0.50 chord line), an assumed rigid-wing span-loading curve, and an estimate of the rigid-wing lift-curve slope.

The portion of the half wing which is elastic (that portion outside of the fuselage) is divided into as many parts as desired. The rigid lift per unit angle of attack of these sections is then estimated from the span loading. The increment in lift due to twist at the section is then assumed to be given by this lift-curve slope multiplied by the twist. Since the twist at a given section depends on the final equilibrium lift at all sections, a set of n simultaneous equations (equal in number to the number of sections the wing is divided into) must be solved; this solution gives the resultant elastic lift at each section. The equations are set up in ratio form with the elastic lift at each section given as a ratio of the rigid lift at the section. The independent variable used in the equations is the rigid lift-curve slope times the dynamic pressure $Cl_{\alpha} q$.

Sketches and equations for the exposed-wing and span-loading curve divided into five sections are given below.



Exposed wing panel divided into five sections.



Span-load curve divided into five sections on exposed wing.

$$L_1 = K' (C_{L\alpha_r})_w q \frac{S}{2} \int_{\eta_{fus. side}}^{\eta_1} \left(\frac{c_l c}{C_L c_{av}} \right)_{rigid} d\eta (\alpha_r + \Delta\alpha_1)$$

$$L_2 = K' (C_{L\alpha_r})_w q \frac{S}{2} \int_{\eta_1}^{\eta_2} \left(\frac{c_l c}{C_L c_{av}} \right)_{rigid} d\eta (\alpha_r + \Delta\alpha_2)$$

.

$$L_5 = K' (C_{L\alpha_r})_w q \frac{S}{2} \int_{\eta_4}^1 \left(\frac{c_l c}{C_L c_{av}} \right)_{rigid} d\eta (\alpha_r + \Delta\alpha_5)$$

$$\left. \begin{aligned}
 \frac{\Delta \alpha_1}{\alpha_r} &= \frac{L_1}{\alpha_r} \theta_{11} + \frac{L_2}{\alpha_r} \theta_{12} + \frac{L_3}{\alpha_r} \theta_{13} + \frac{L_4}{\alpha_r} \theta_{14} + \frac{L_5}{\alpha_r} \theta_{15} \\
 \frac{\Delta \alpha_2}{\alpha_r} &= \frac{L_1}{\alpha_r} \theta_{21} + \frac{L_2}{\alpha_r} \theta_{22} + \frac{L_3}{\alpha_r} \theta_{23} + \frac{L_4}{\alpha_r} \theta_{24} + \frac{L_5}{\alpha_r} \theta_{25} \\
 &\cdot \quad \cdot \quad \cdot \quad \cdot \quad \cdot \quad \cdot \quad \cdot \\
 \frac{\Delta \alpha_5}{\alpha_r} &= \frac{L_1}{\alpha_r} \theta_{51} + \frac{L_2}{\alpha_r} \theta_{52} + \frac{L_3}{\alpha_r} \theta_{53} + \frac{L_4}{\alpha_r} \theta_{54} + \frac{L_5}{\alpha_r} \theta_{55}
 \end{aligned} \right\} \quad (4)$$

When equations (3) are substituted into equations (4) for $\Delta \alpha_1/\alpha_r$, $\Delta \alpha_2/\alpha_r$, . . . $\Delta \alpha_5/\alpha_r$, the following set of five simultaneous equations is obtained with $(C_{L_{\alpha_r}})_w q = Q$ as the independent variable:

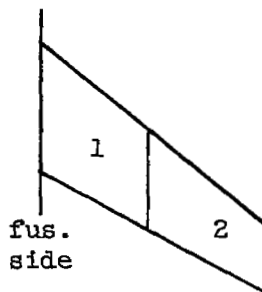
$$\left. \begin{aligned}
 \frac{L_1}{\alpha_r} \left(\theta_{11} - \frac{1}{K_1 Q} \right) + \frac{L_2}{\alpha_r} \theta_{12} + \frac{L_3}{\alpha_r} \theta_{13} + \frac{L_4}{\alpha_r} \theta_{14} + \frac{L_5}{\alpha_r} \theta_{15} &= -1 \\
 \frac{L_1}{\alpha_r} \theta_{21} + \frac{L_2}{\alpha_r} \left(\theta_{22} - \frac{1}{K_2 Q} \right) + \frac{L_3}{\alpha_r} \theta_{23} + \frac{L_4}{\alpha_r} \theta_{24} + \frac{L_5}{\alpha_r} \theta_{25} &= -1 \\
 \frac{L_1}{\alpha_r} \theta_{31} + \frac{L_2}{\alpha_r} \theta_{32} + \frac{L_3}{\alpha_r} \left(\theta_{33} - \frac{1}{K_3 Q} \right) + \frac{L_4}{\alpha_r} \theta_{34} + \frac{L_5}{\alpha_r} \theta_{35} &= -1 \\
 \frac{L_1}{\alpha_r} \theta_{41} + \frac{L_2}{\alpha_r} \theta_{42} + \frac{L_3}{\alpha_r} \theta_{43} + \frac{L_4}{\alpha_r} \left(\theta_{44} - \frac{1}{K_4 Q} \right) + \frac{L_5}{\alpha_r} \theta_{45} &= -1 \\
 \frac{L_1}{\alpha_r} \theta_{51} + \frac{L_2}{\alpha_r} \theta_{52} + \frac{L_3}{\alpha_r} \theta_{53} + \frac{L_4}{\alpha_r} \theta_{54} + \frac{L_5}{\alpha_r} \left(\theta_{55} - \frac{1}{K_5 Q} \right) &= -1
 \end{aligned} \right\} \quad (5)$$

After equations (5) are solved for L_1/α_r , L_2/α_r . . . L_5/α_r for each value of Q ,

$$\left(\frac{C_{I\alpha_e}}{C_{I\alpha_r}} \right)_w = \frac{2 \left(\frac{L_1}{\alpha_r} + \frac{L_2}{\alpha_r} + \frac{L_3}{\alpha_r} + \frac{L_4}{\alpha_r} + \frac{L_5}{\alpha_r} \right)}{QS} \quad (6)$$

for the exposed wing.

The effect of wing-inertia loading acting in opposition to aerodynamic loading has been neglected in equations (5). The addition of a wing-inertia term for a case where the wing is divided into two sections is illustrated as follows:



$$\left. \begin{aligned} \frac{\Delta\alpha_1}{\alpha_r} &= \frac{L_1}{\alpha_r} \theta_{11} + \frac{L_2}{\alpha_r} \theta_{12} - \frac{1}{W} \frac{L_T}{\alpha_r} (W_1 \theta_{11} + W_2 \theta_{12}) = \frac{1}{K_1 Q} \frac{L_1}{\alpha_r} - 1 \\ \frac{\Delta\alpha_2}{\alpha_r} &= \frac{L_1}{\alpha_r} \theta_{21} + \frac{L_2}{\alpha_r} \theta_{22} - \frac{1}{W} \frac{L_T}{\alpha_r} (W_1 \theta_{21} + W_2 \theta_{22}) = \frac{1}{K_2 Q} \frac{L_2}{\alpha_r} - 1 \end{aligned} \right\} \quad (7)$$

where

- W total model weight
- W₁ weight of inboard section of exposed half-wing
- W₂ weight of outboard section of exposed half-wing
- L_T total lift of model

The inboard movement in the spanwise center of pressure which results from the reduction in lift due to aeroelastic wing twist causes a change in aerodynamic-center position. The lateral center of pressure of the exposed elastic wing can be found from L_1/α_r , L_2/α_r , . . . L_5/α_r solved from the simultaneous equations (5) as follows:

$$(y'_{cp})_e = \frac{L_1 y_1' + L_2 y_2' + L_3 y_3' + L_4 y_4' + L_5 y_5'}{L_1 + L_2 + L_3 + L_4 + L_5}$$

If the span load is assumed to move inboard along the half- or quarter-chord line, the increment in aerodynamic-center position of the complete model due to the inboard movement can be found from the following expression:

$$\Delta \frac{\partial C_m}{\partial C_L} = \left[\frac{(y'_{cp})_r - (y'_{cp})_e}{\bar{c}} \tan \Lambda \right] \frac{C_{L\alpha_w}}{C_{L\alpha_{total}}} \quad (9)$$

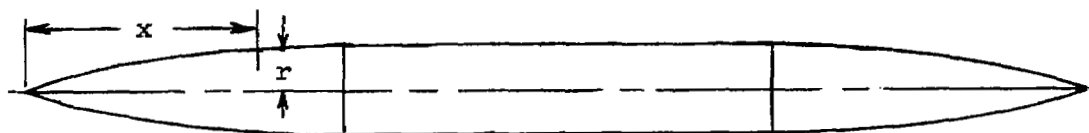
For the $\tan \Lambda$ use either $\tan \Lambda_c/4$ or $\tan \Lambda_c/2$ whichever is appropriate.

REFERENCES

1. Gillis, Clarence L., Peck, Robert F., and Vitale, A. James: Preliminary Results From a Free-Flight Investigation at Transonic and Supersonic Speeds of the Longitudinal Stability and Control Characteristics of an Airplane Configuration With a Thin Straight Wing of Aspect Ratio 3. NACA RM L9K25a, 1950.
2. Gillis, Clarence L., and Vitale, A. James: Wing-On and Wing-Off Longitudinal Characteristics of an Airplane Configuration Having a Thin Unswept Tapered Wing of Aspect Ratio 3, As Obtained From Rocket-Propelled Models at Mach Numbers From 0.8 to 1.4. NACA RM L50K16, 1951.
3. Vitale, A. James, McFall, John C., Jr., and Morrow, John D.: Longitudinal Stability and Drag Characteristics at Mach Numbers From 0.75 to 1.5 of an Airplane Configuration Having a 60° Swept Wing of Aspect Ratio 2.24 as Obtained From Rocket-Propelled Models. NACA RM L51K06, 1952.
4. Chapman, Rowe, Jr., and Morrow, John D.: Longitudinal Stability and Drag Characteristics at Mach Numbers From 0.70 to 1.37 of Rocket-Propelled Models Having a Modified Triangular Wing. NACA RM L52A31, 1952.
5. McFall, John C., Jr., and Hollinger, James A.: Longitudinal Stability, Control Effectiveness, and Drag Characteristics at Transonic Speeds of a Rocket-Propelled Model of an Airplane Configuration Having an Unswept Tapered Wing of Aspect Ratio 3.0 and NACA 65A004.5 Airfoil Sections. NACA RM L52L04, 1952.
6. Peck, Robert F., and Mitchell, Jesse L.: Rocket-Model Investigation of Longitudinal Stability and Drag Characteristics of an Airplane Configuration Having a 60° Delta Wing and a High Unswept Horizontal Tail. NACA RM L52K04a, 1952.
7. Mitchell, Jesse L., and Peck, Robert F.: An NACA Vane-Type Angle-of-Attack Indicator for Use at Subsonic and Supersonic Speeds. NACA RM L9F28a, 1949.
8. Osborne, Robert S.: A Transonic-Wing Investigation in the Langley 8-Foot High-Speed Tunnel at High Subsonic Mach Numbers and at a Mach Number of 1.2. Wing-Fuselage Configuration Having a Wing of 45° Sweepback, Aspect Ratio 4, Taper Ratio 0.6, and NACA 65A006 Airfoil Section. NACA RM L50H08, 1950.

9. Cahill, Jones F., and Gottlieb, Stanley M.: Low-Speed Aerodynamic Characteristics of a Series of Swept Wings Having NACA 65A006 Airfoil Sections (Revised). NACA RM L50F16, 1950.
10. Parks, James H., and Kehlet, Alan B.: Longitudinal Stability, Trim, and Drag Characteristics of a Rocket-Propelled Model of an Airplane Configuration Having a 45° Sweptback Wing and an Unswept Horizontal Tail. NACA RM L52F05, 1952.
11. DeYoung, John, and Harper, Charles W.: Theoretical Symmetric Span Loading at Subsonic Speeds for Wings Having Arbitrary Plan Form. NACA Rep. 921, 1948.
12. Loving, Donald L., and Williams, Claude V.: Aerodynamic Loading Characteristics of a Wing-Fuselage Combination Having a Wing of 45° Sweepback Measured in the Langley 8-Foot Transonic Tunnel. NACA RM L52B27, 1952.
13. Diederich, Franklin W., and Foss, Kenneth A.: Charts and Approximate Formulas for the Estimation of Aeroelastic Effects on the Loading of Swept and Unswept Wings. NACA TN 2608, 1952.
14. Osborne, Robert S., and Mugler, John P., Jr.: Effects of Wing Elasticity on the Aerodynamic Characteristics of a 45° Sweptback-Wing-Fuselage Combination Measured in the Langley 8-Foot Transonic Tunnel. NACA RM L52G23, 1952.
15. Mitchell, Jesse L.: The Static and Dynamic Longitudinal Stability Characteristics of Some Supersonic Aircraft Configurations. NACA RM L52A10a, 1952.
16. Langley Pilotless Aircraft Research Division: Some Recent Data From Flight Tests of Rocket-Powered Models. NACA RM L50K24, 1951.

TABLE I.- FUSELAGE NOSE AND TAIL ORDINATES FOR AIRPLANE CONFIGURATION



x, in.	r, in.
0	0.168
0.060	.182
.122	.210
.245	.224
.480	.294
.735	.350
1.225	.462
2.000	.639
2.450	.735
4.800	1.245
7.350	1.721
8.000	1.849
9.800	2.155
12.250	2.505
13.125	2.608
14.375	2.747
14.700	2.785
17.150	3.010
19.600	3.220
22.050	3.385
24.500	3.500



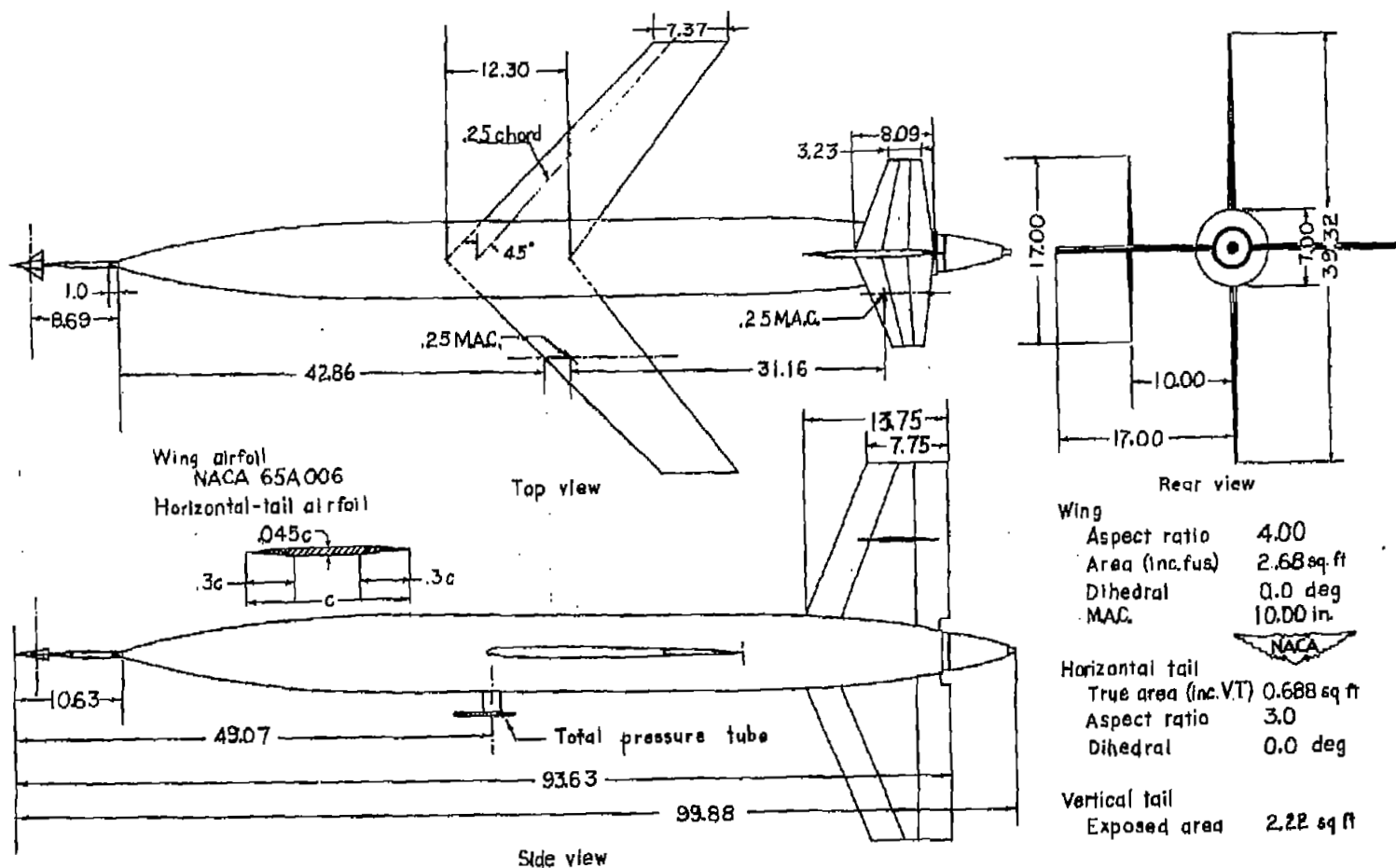
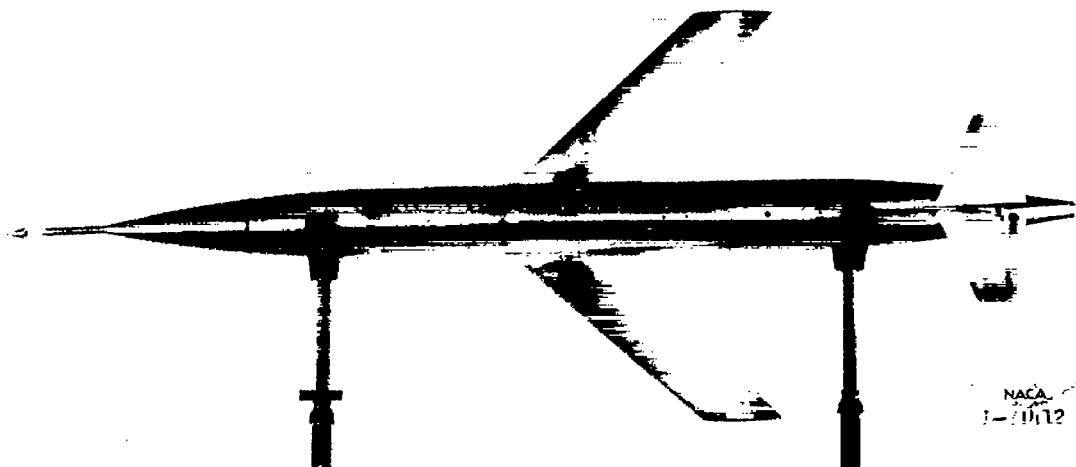
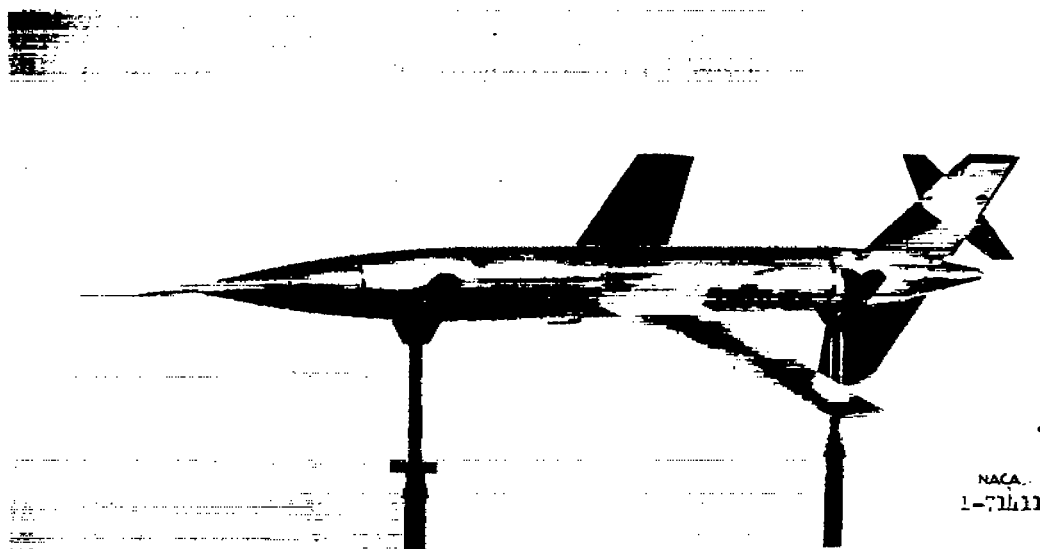


Figure 1.- General arrangement of model. All dimensions are in inches.

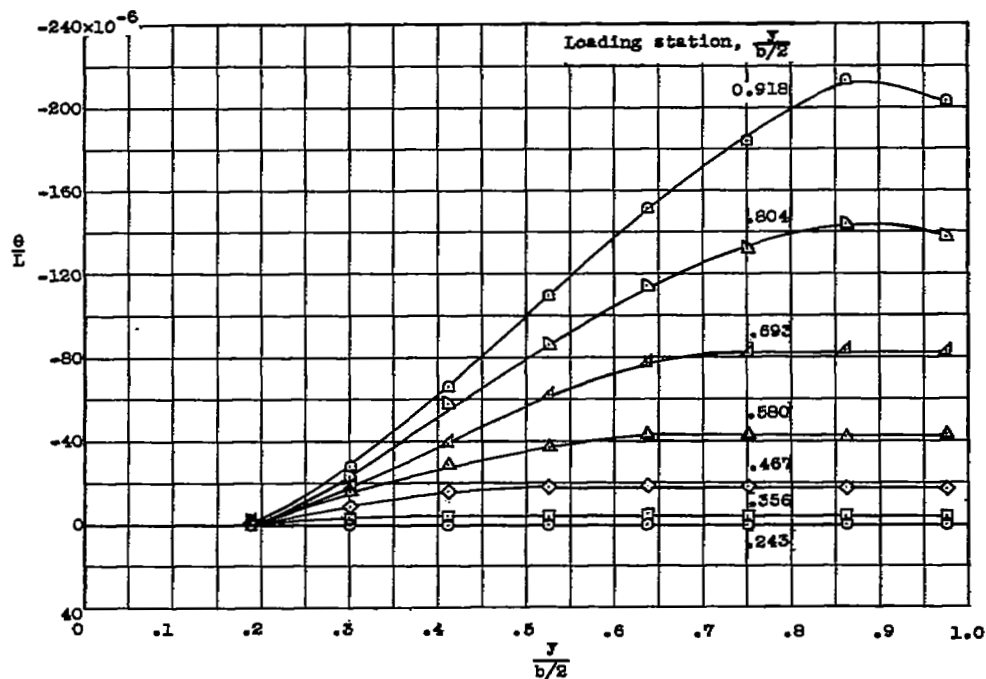


(a) Top view.

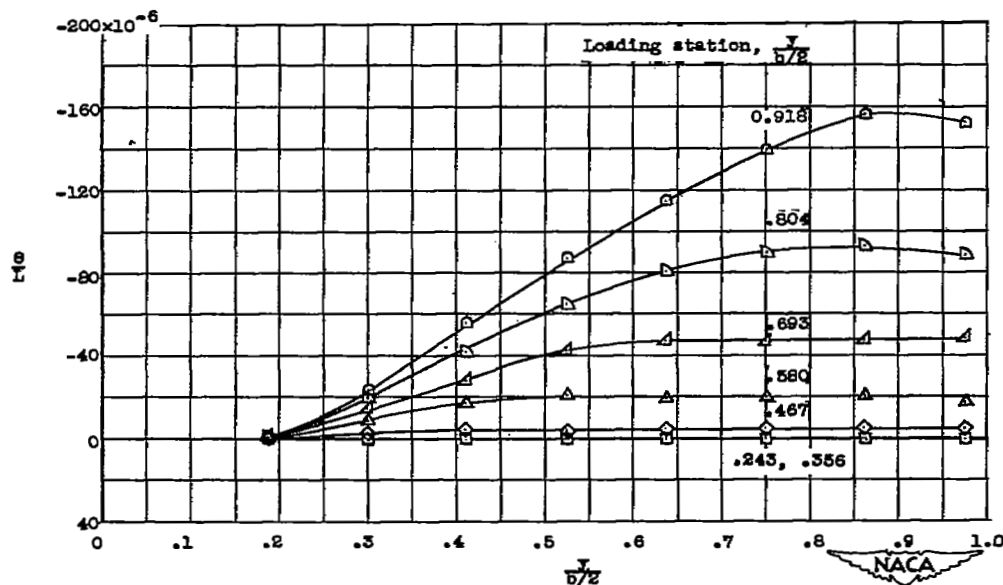


(b) Three-quarter front view.

Figure 2.- Photographs of duralumin-wing model.

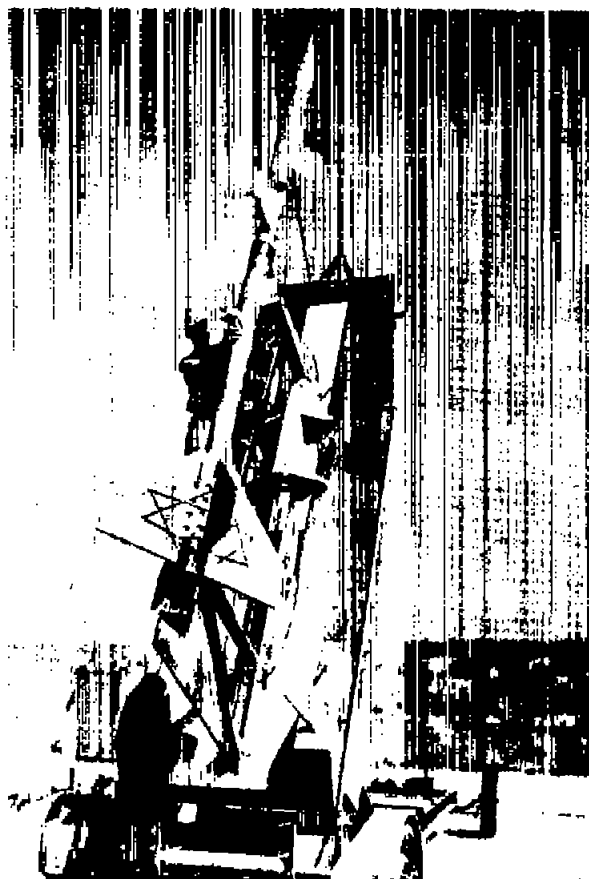



(a) Load applied along the 50-percent chord line.

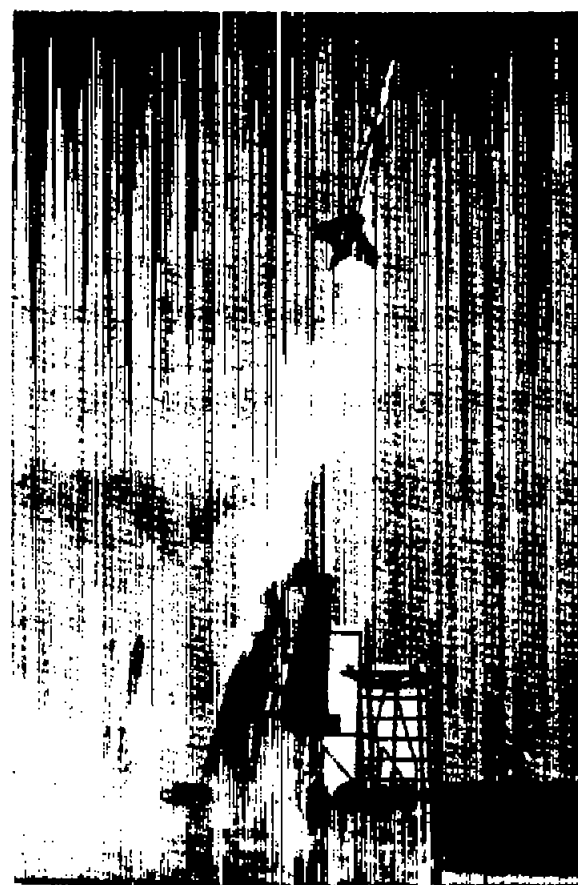


(b) Load applied along the 25-percent chord line.

Figure 3.- Twist in the free-stream direction per unit load applied at various stations along the span of the duralumin wing.



(a) Before launching. 
L-71584




(b) After launching. 
L-77899

Figure 4.- Model launching.

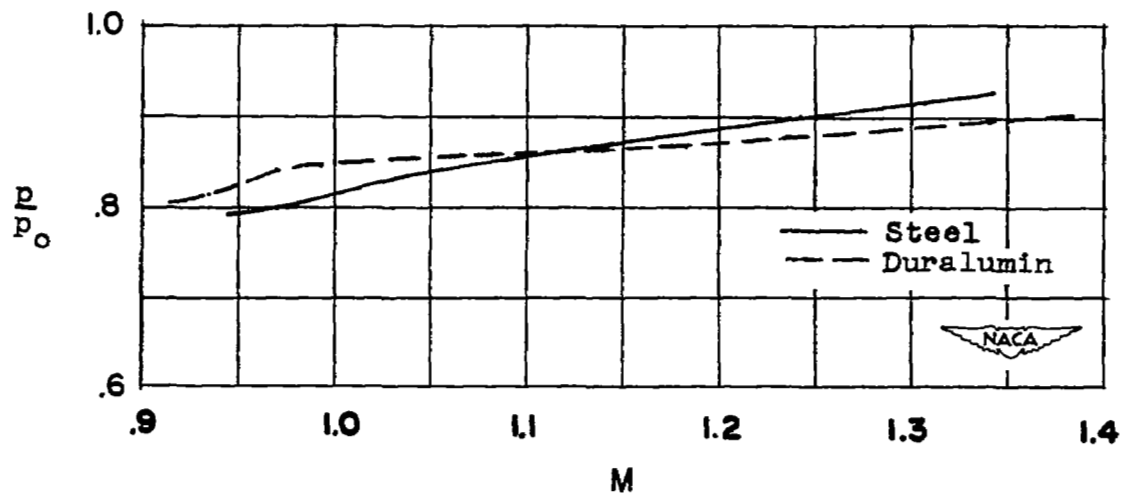


Figure 5.- Static-pressure ratio.

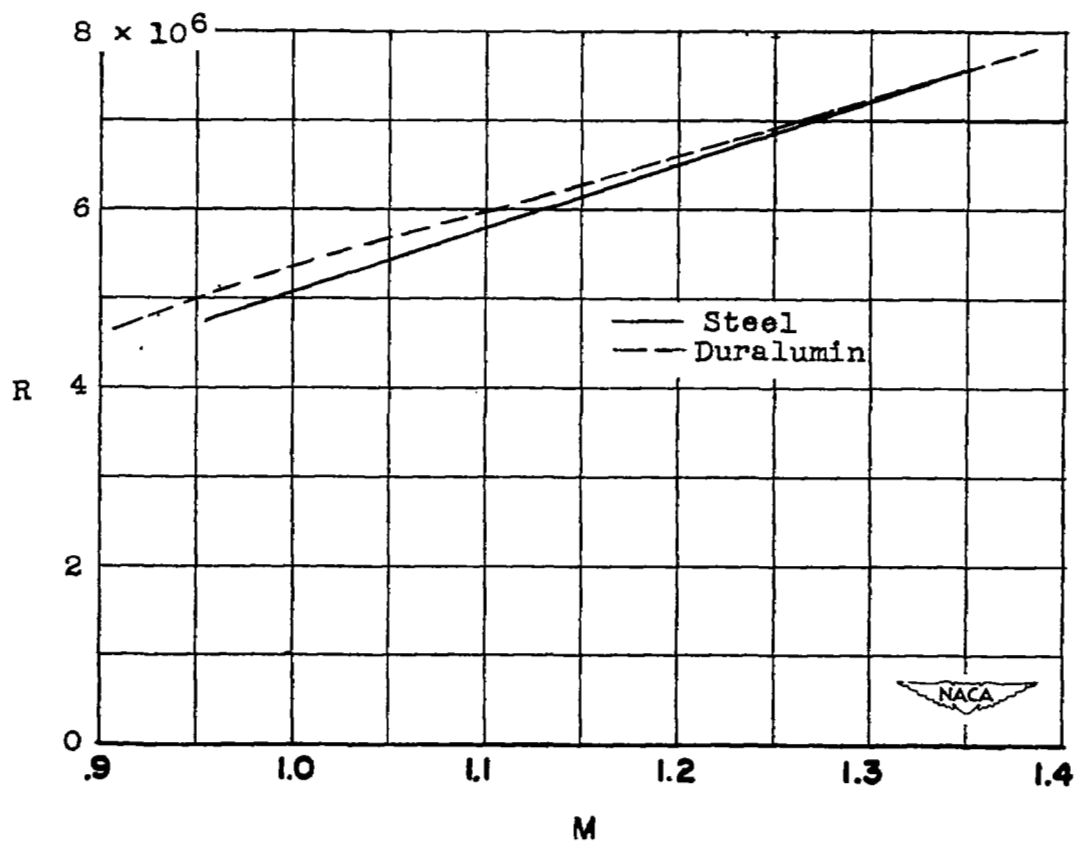
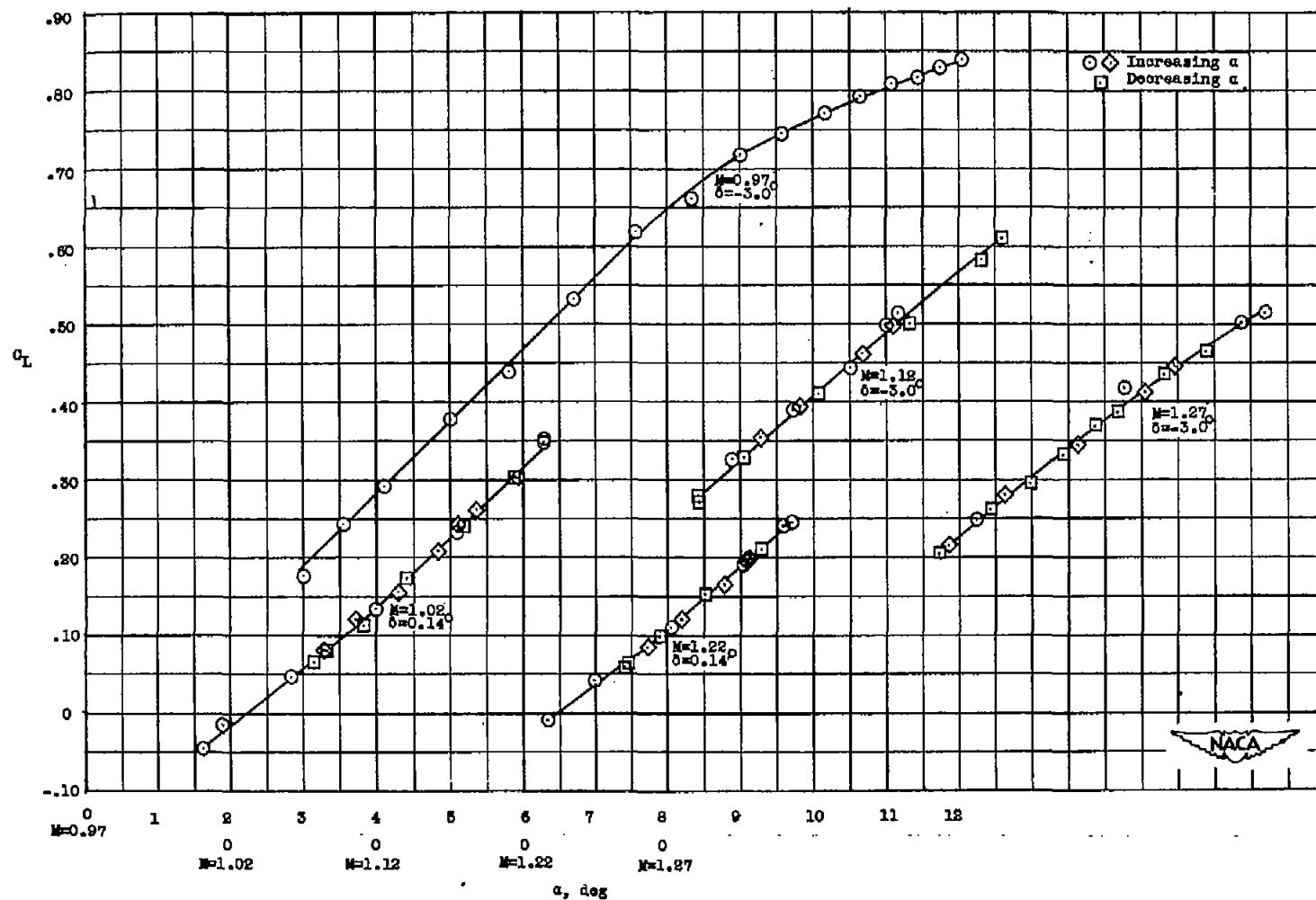
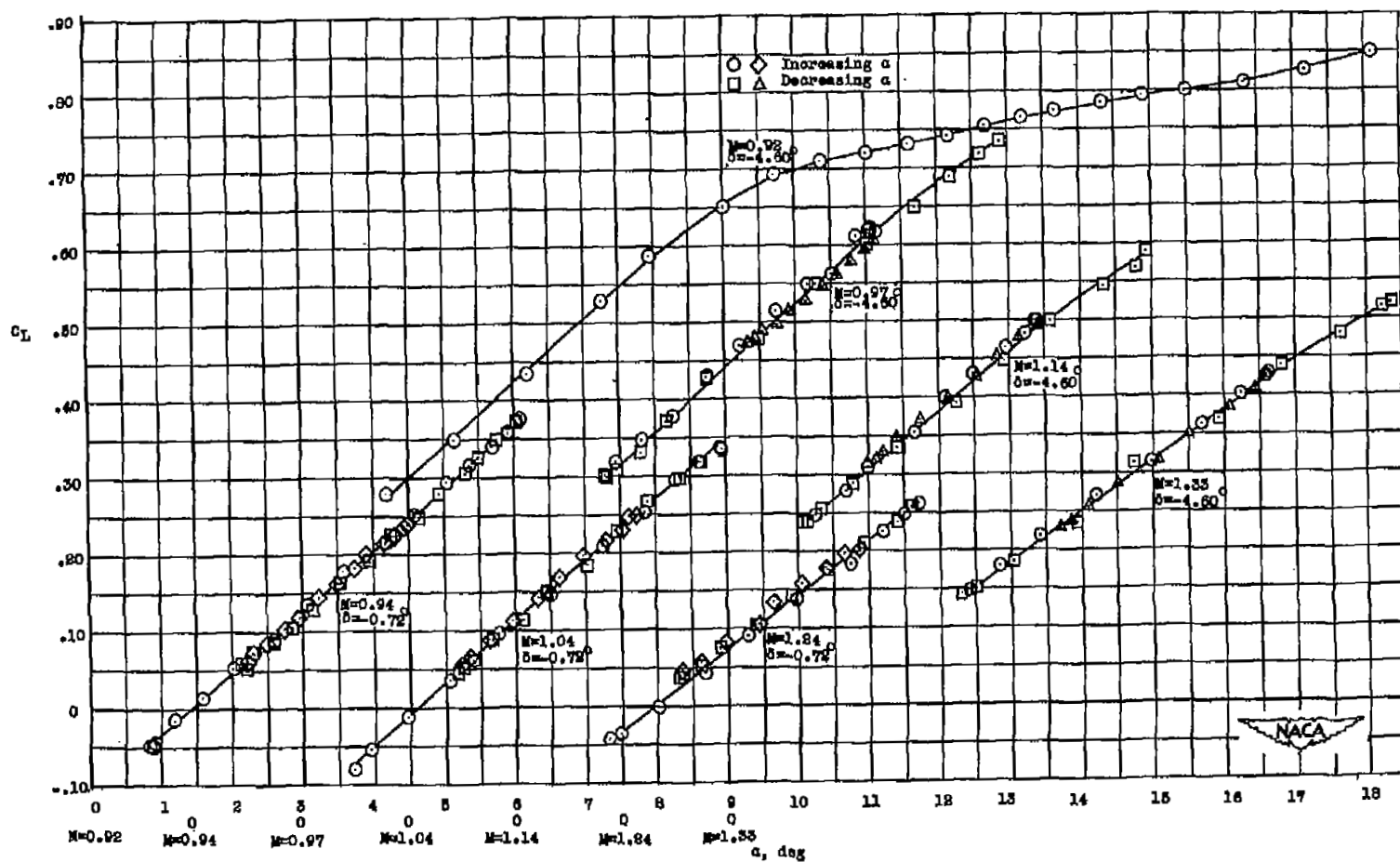


Figure 6.- Reynolds number of tests, based on mean aerodynamic chords.



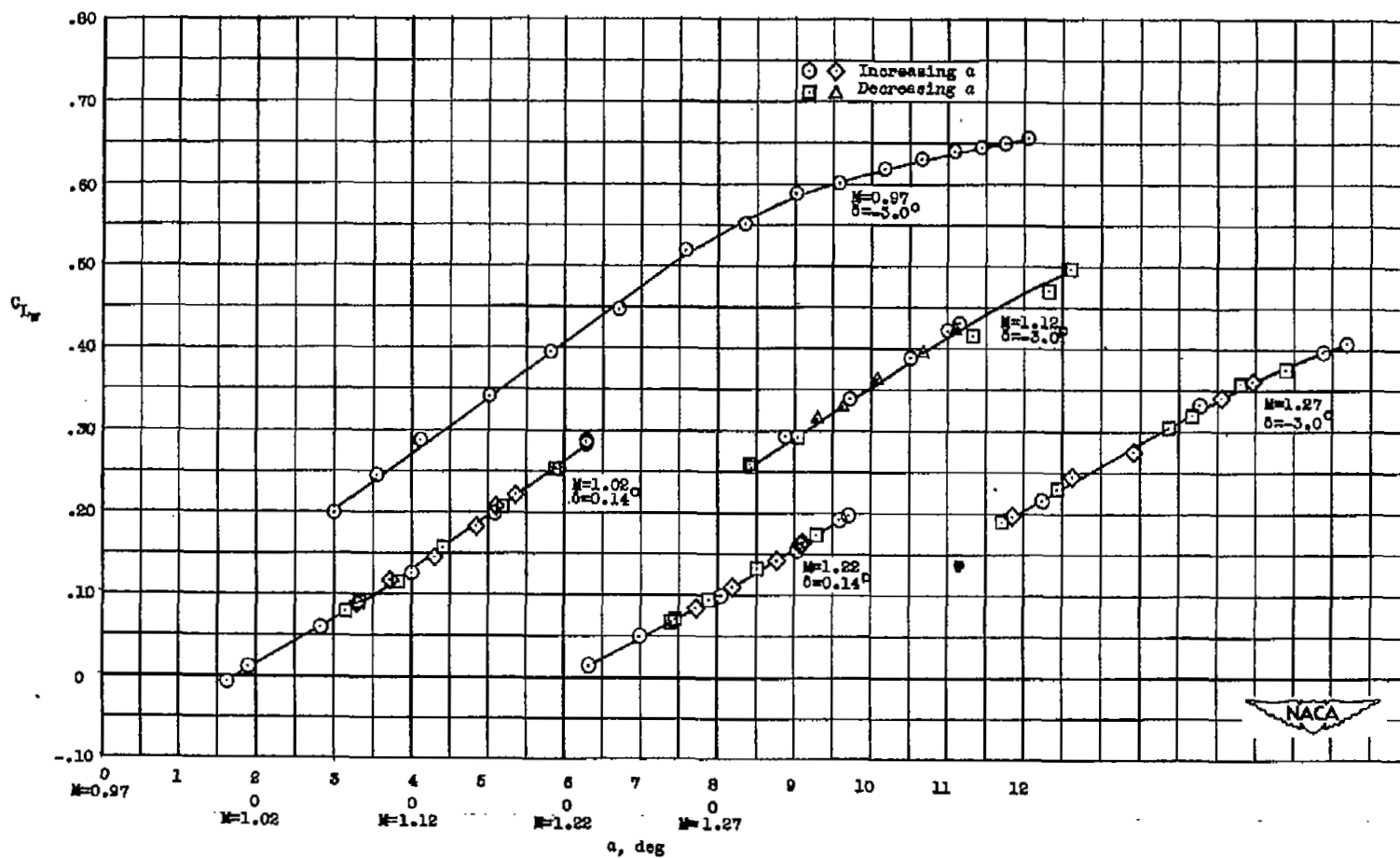
(a) Steel-wing model.

Figure 7.- Lift data for complete models.



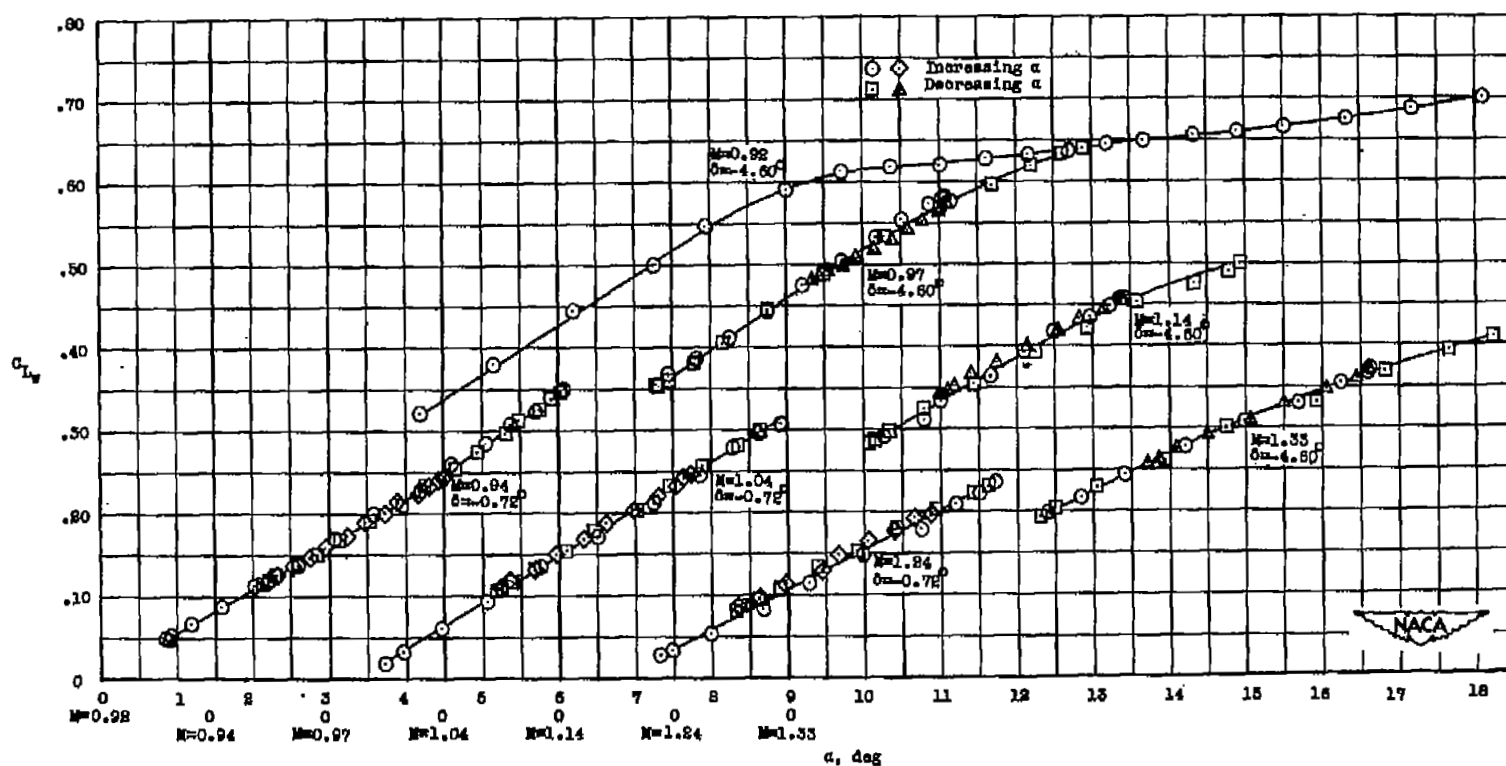
(b) Duralumin wing model.

Figure 7.- Concluded.



(a) Steel wing.

Figure 8.- Lift data for exposed wings.



(b) Duralumin wing.

Figure 8.- Concluded.

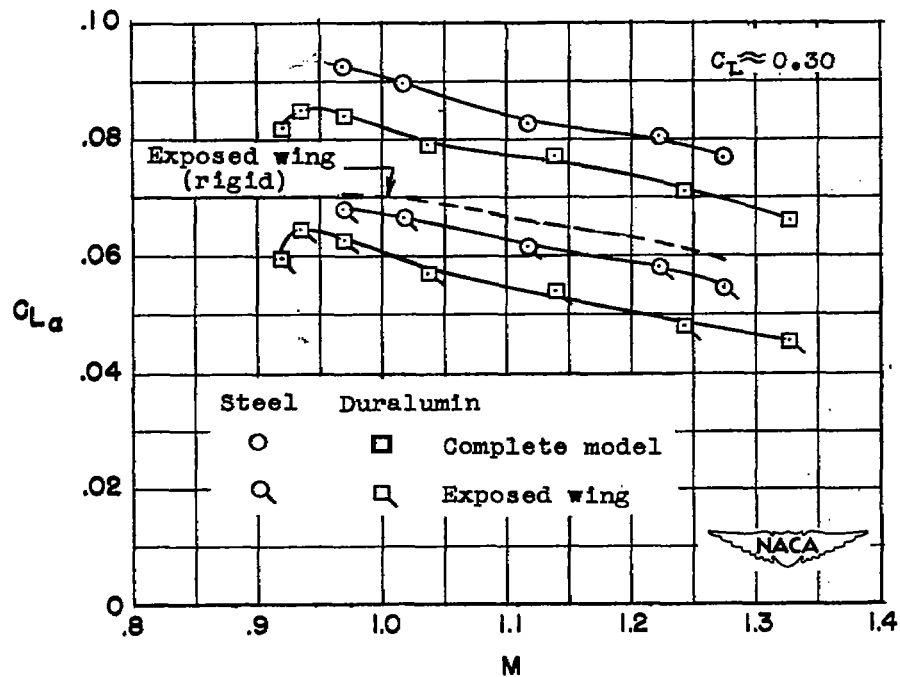


Figure 9.- Lift-curve slopes.

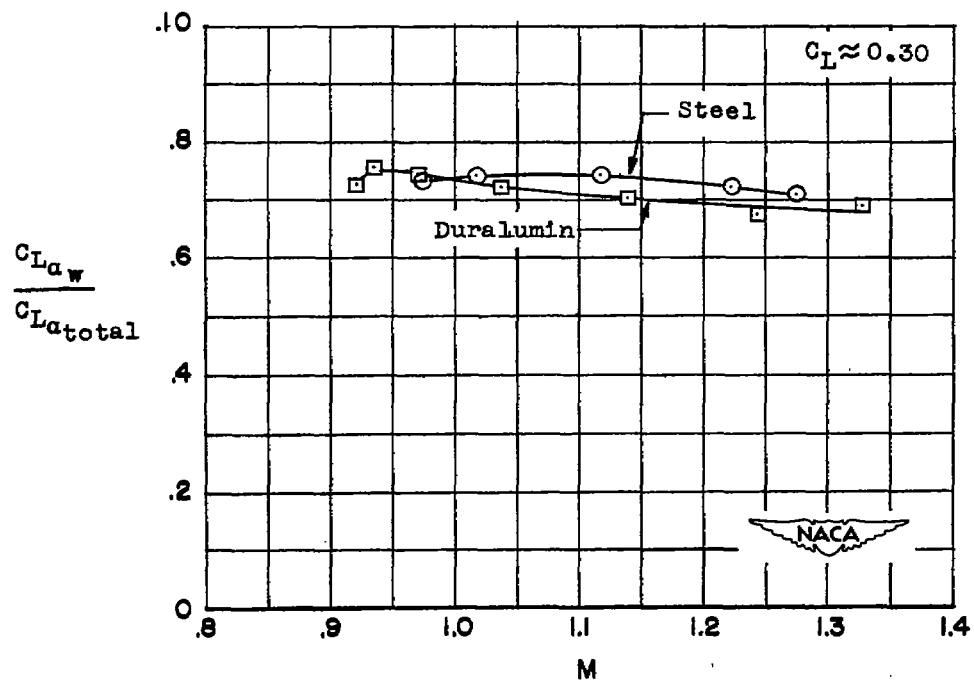


Figure 10.- Rate of change of exposed-wing lift with complete model lift.

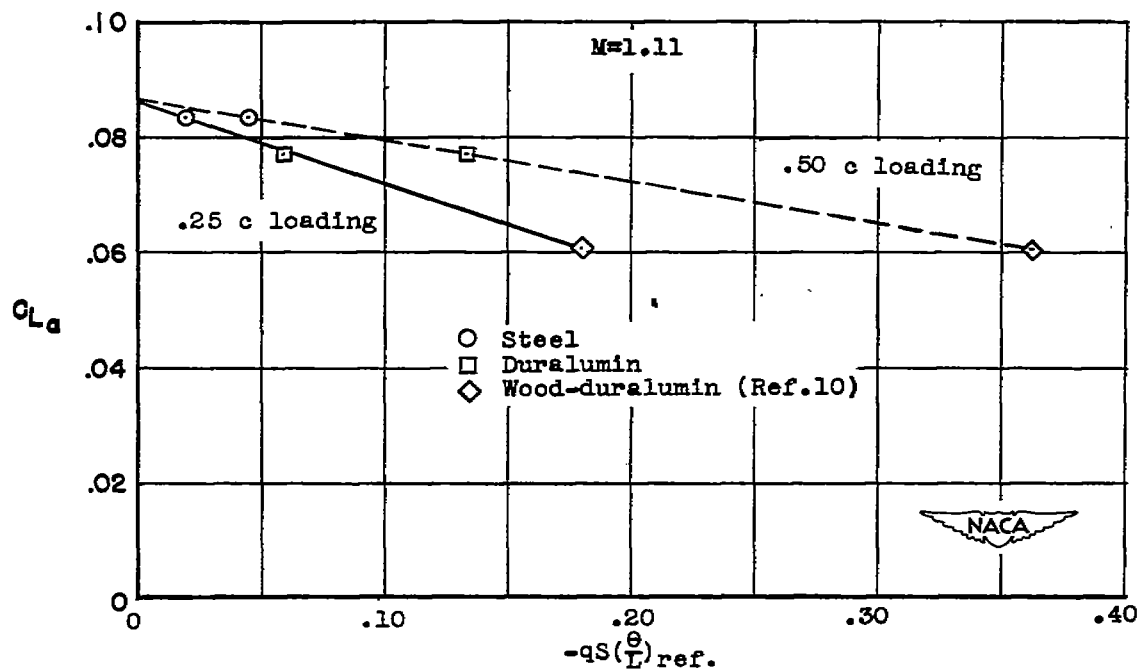


Figure 11.- Variation of complete model lift-curve slope with wing stiffness at $M = 1.11$.

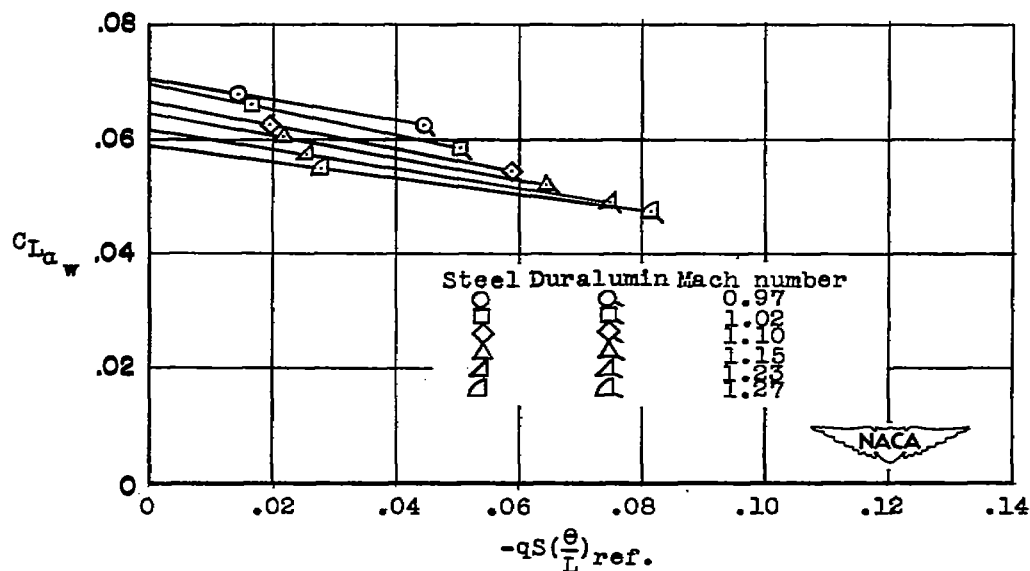


Figure 12.- Extrapolation between steel and duralumin exposed-wing lift-curve slopes to obtain rigid values.

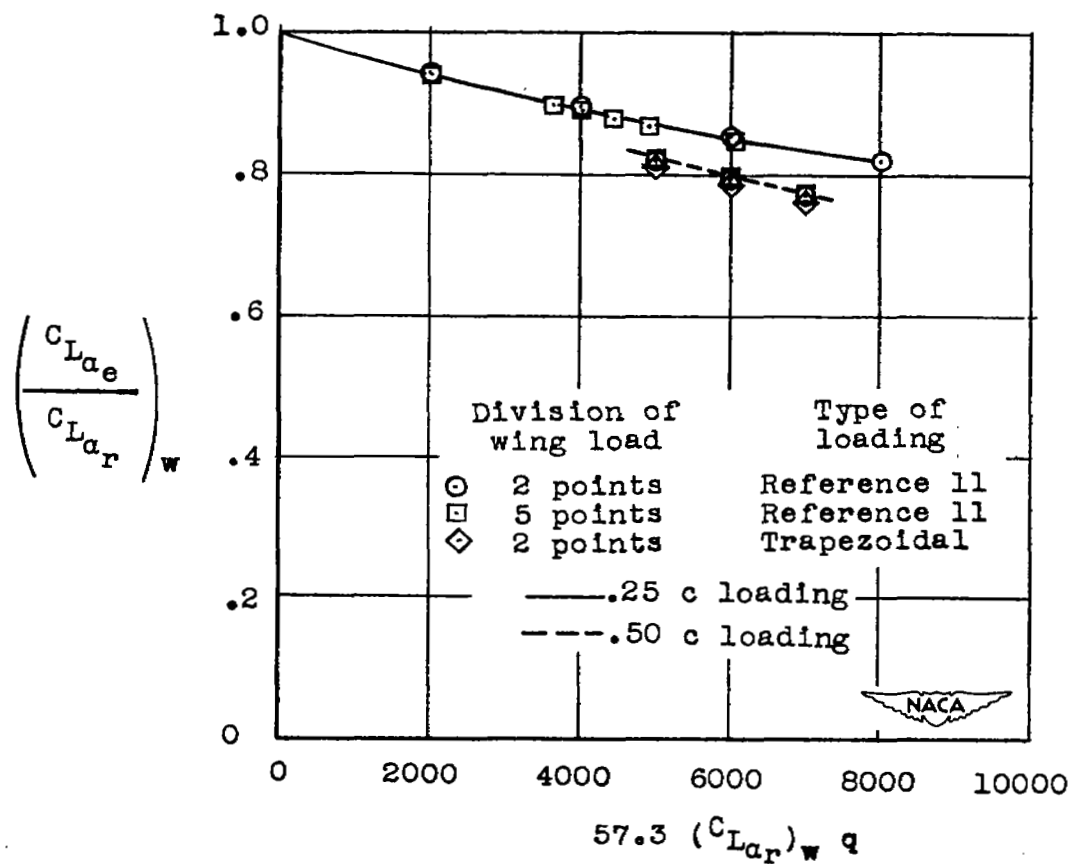


Figure 13.- Ratio of elastic- to rigid-exposed-wing lift-curve slopes calculated by the method of the appendix for the duralumin wing.

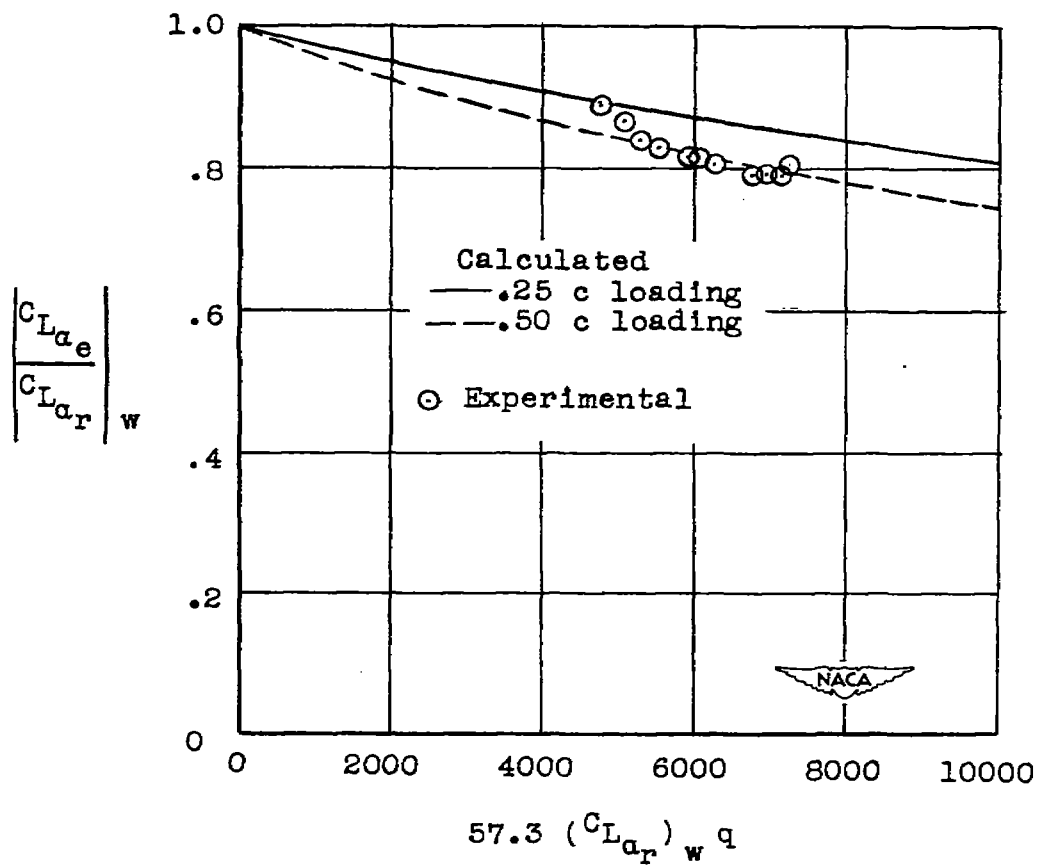
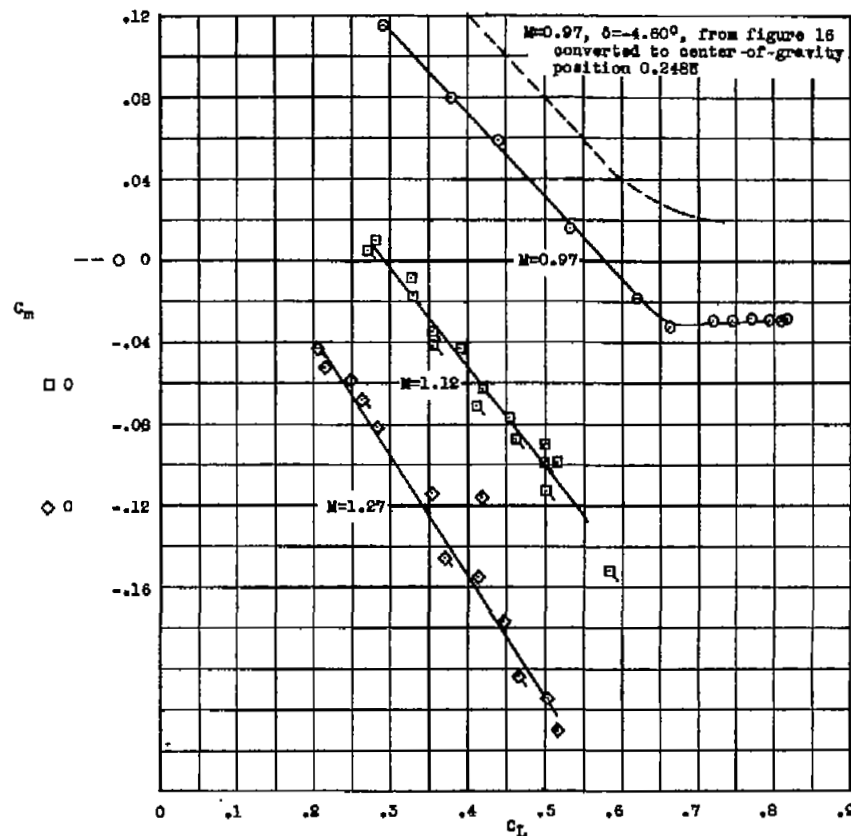
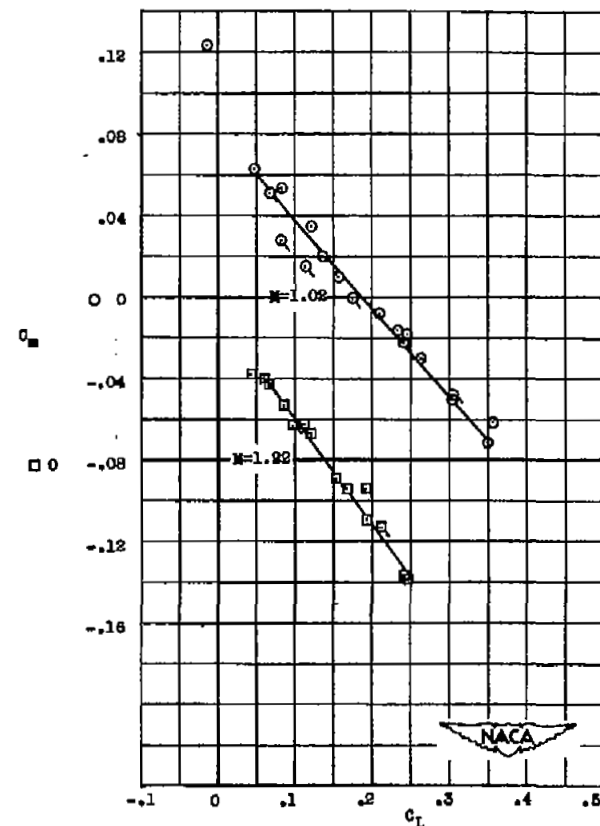


Figure 14.- Comparison between experimental and calculated elastic- to rigid-lift-curve-slope ratios for the duralumin wing.

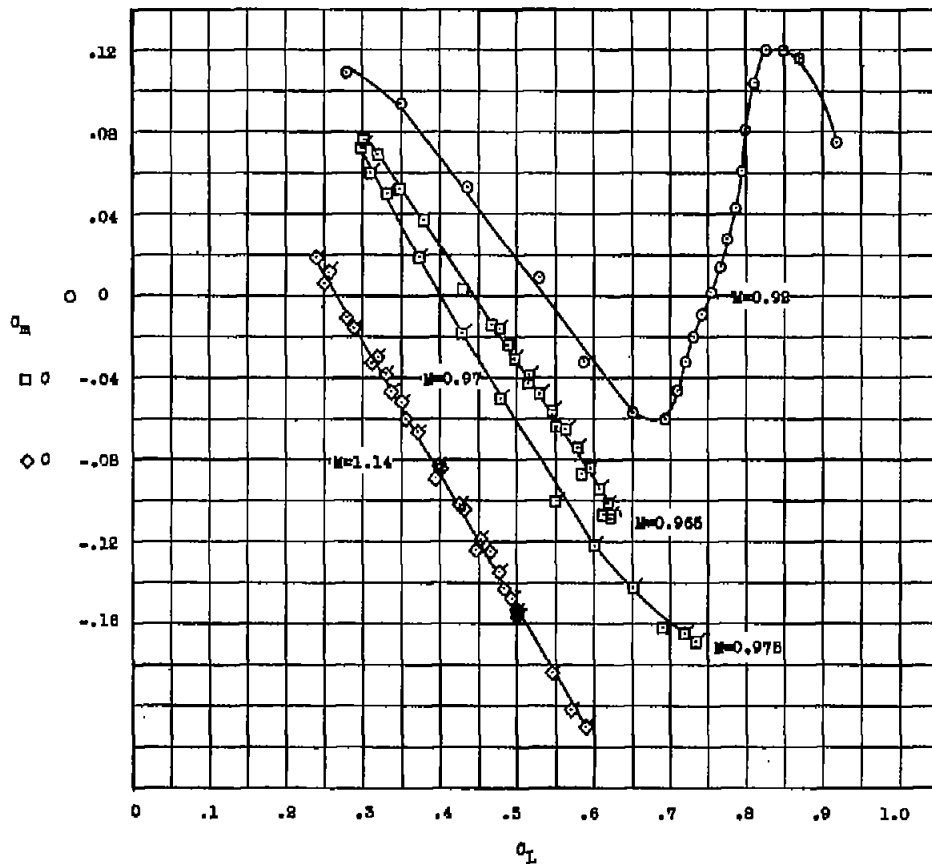


(a) Horizontal-tail deflection,
-3.0°

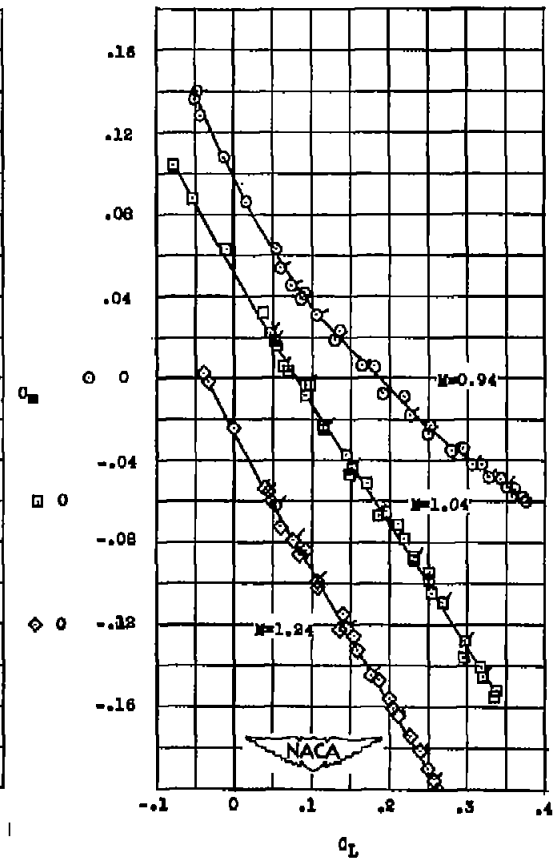


(b) Horizontal-tail deflection,
0.14°

Figure 15.- Pitching-moment data for the steel-wing model about a center-of-gravity position 24.8 percent of the mean aerodynamic chord as obtained from the double differentiation method. Flagged symbols indicate decreasing C_L .

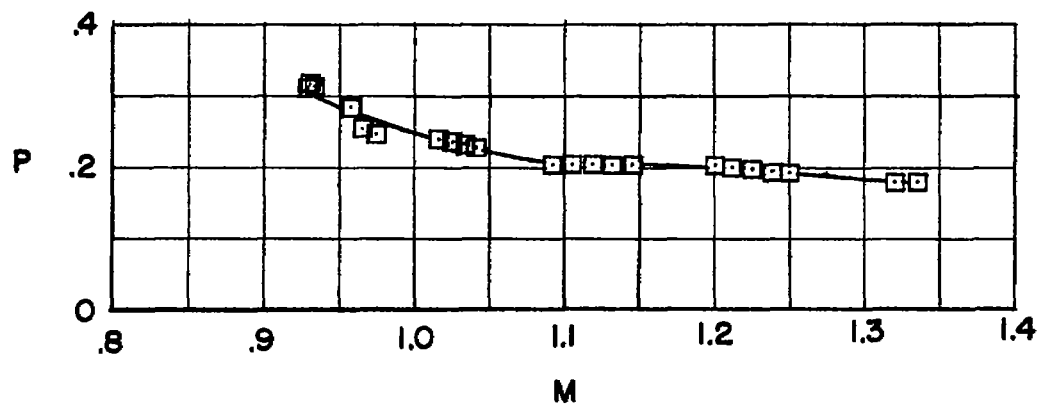


(a) Horizontal tail deflection,
-4.60°.

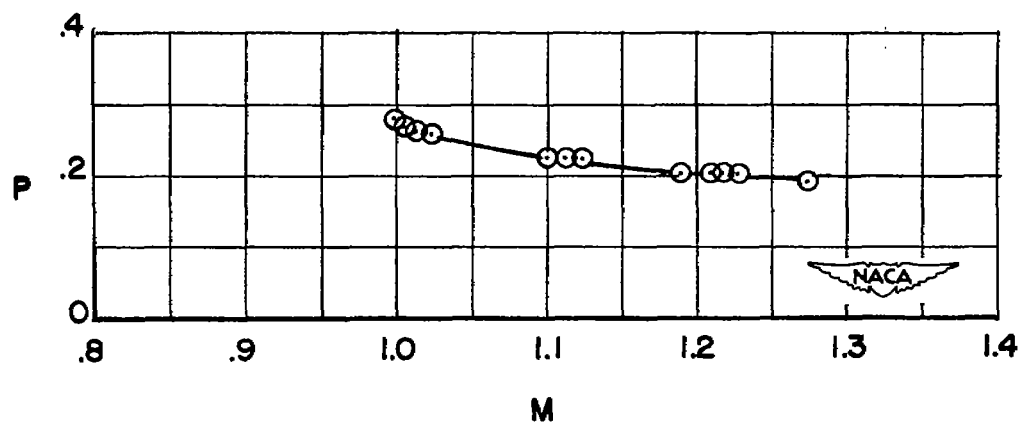


(b) Horizontal tail deflection,
-0.72°.

Figure 16.- Pitching-moment data for the duralumin-wing model about a center-of-gravity position 4.60 percent of the mean aerodynamic chord as obtained from the double accelerometer method. Flagged symbols indicate decreasing C_L .



(a) Duralumin-wing model; center-of-gravity position, 4.60 percent mean aerodynamic chord.



(b) Steel-wing model; center-of-gravity position, 24.8 percent mean aerodynamic chord.

Figure 17.- Period of oscillations.

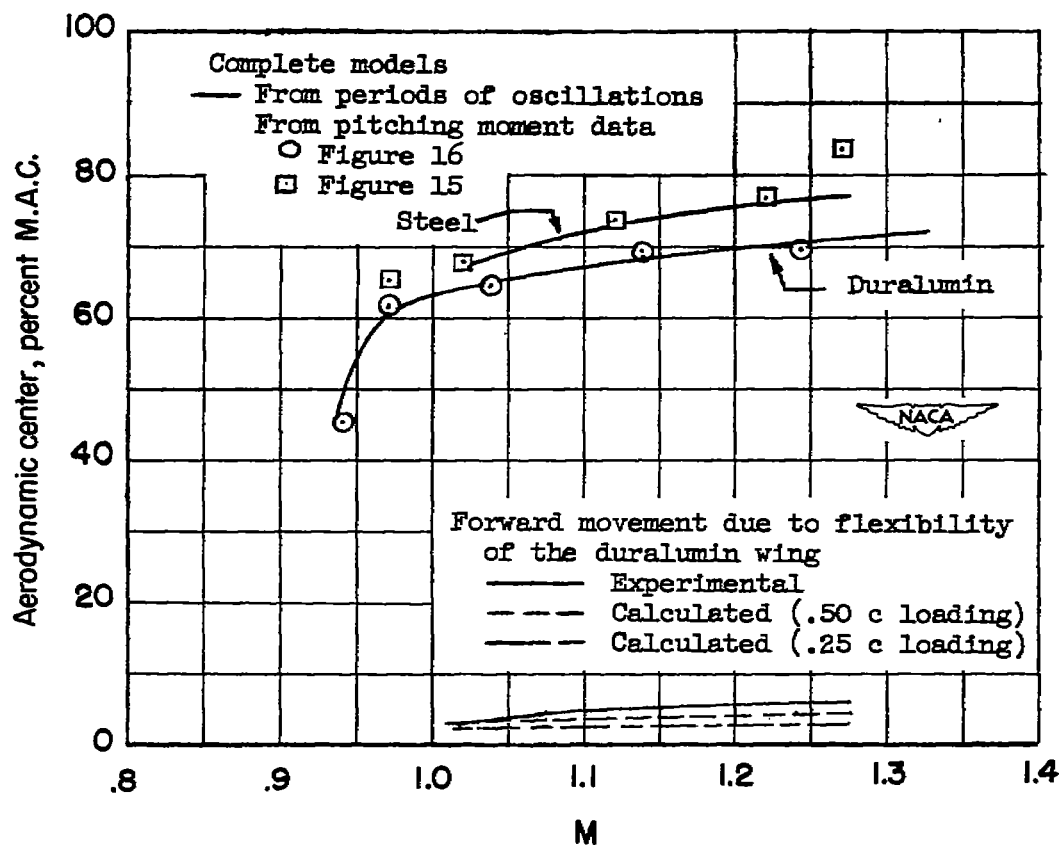
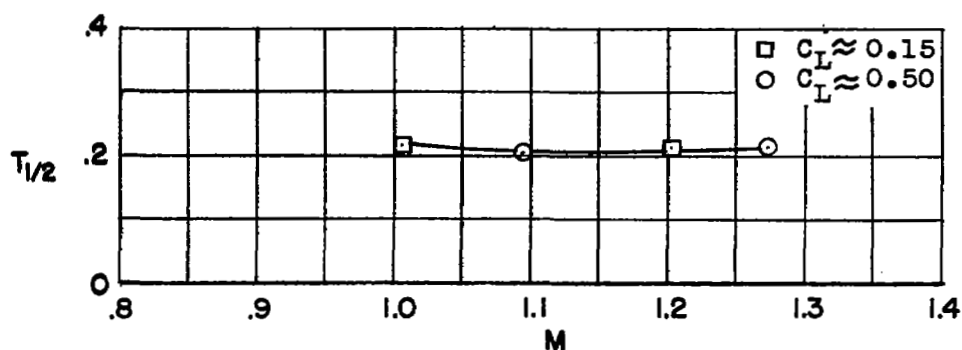
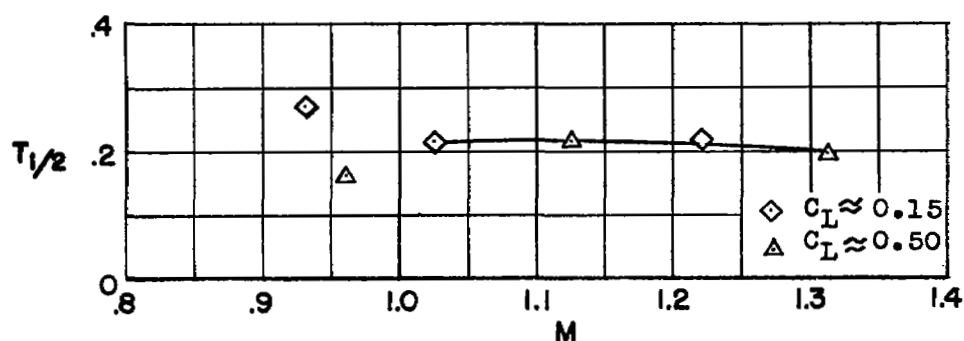


Figure 18.- Variation of aerodynamic-center position with Mach number.



(a) Steel-wing-model time to damp to one-half amplitude.



(b) Duralumin-wing-model time to damp to one-half amplitude.

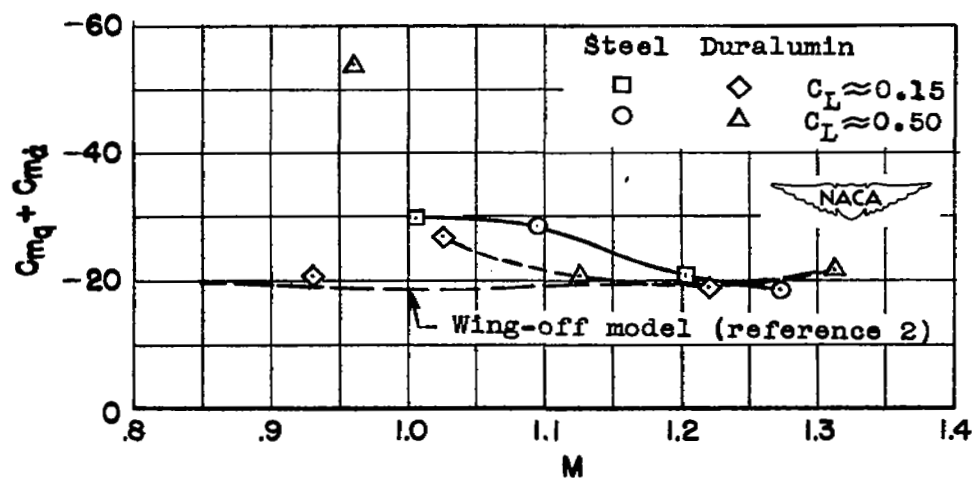
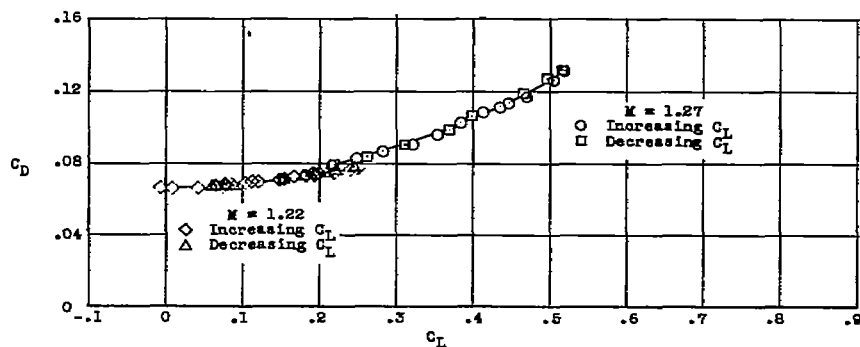
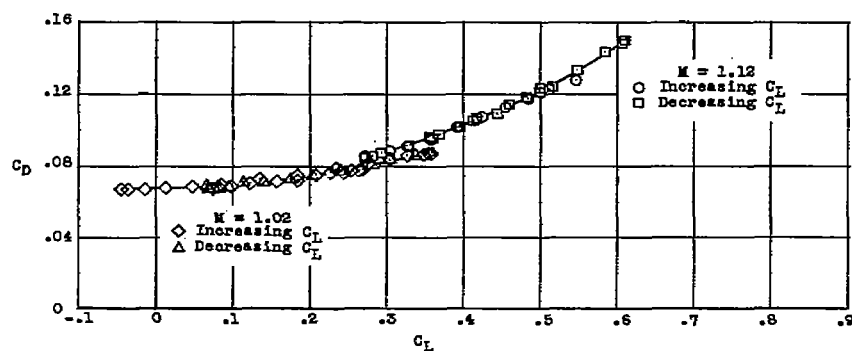
(c) Pitching-moment damping derivative $C_{mq} + C_{m\dot{\alpha}}$.

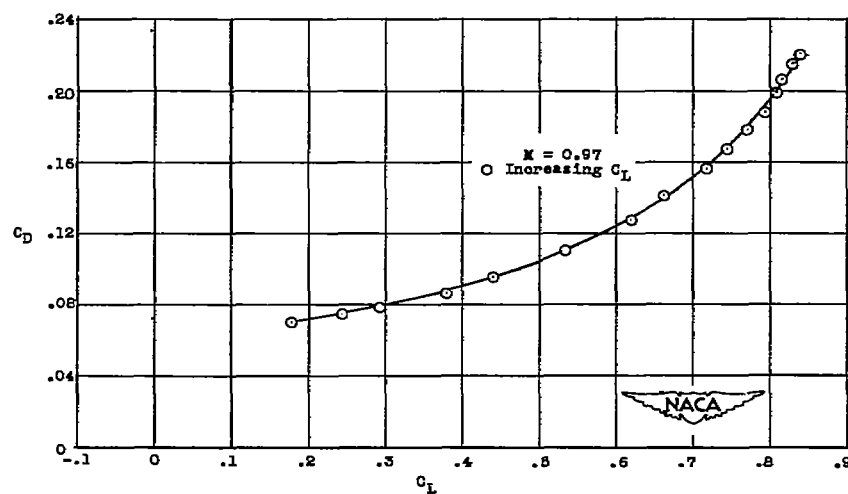
Figure 19.- Damping characteristics of the short-period oscillations.



(a) Mach numbers 1.27 and 1.22.

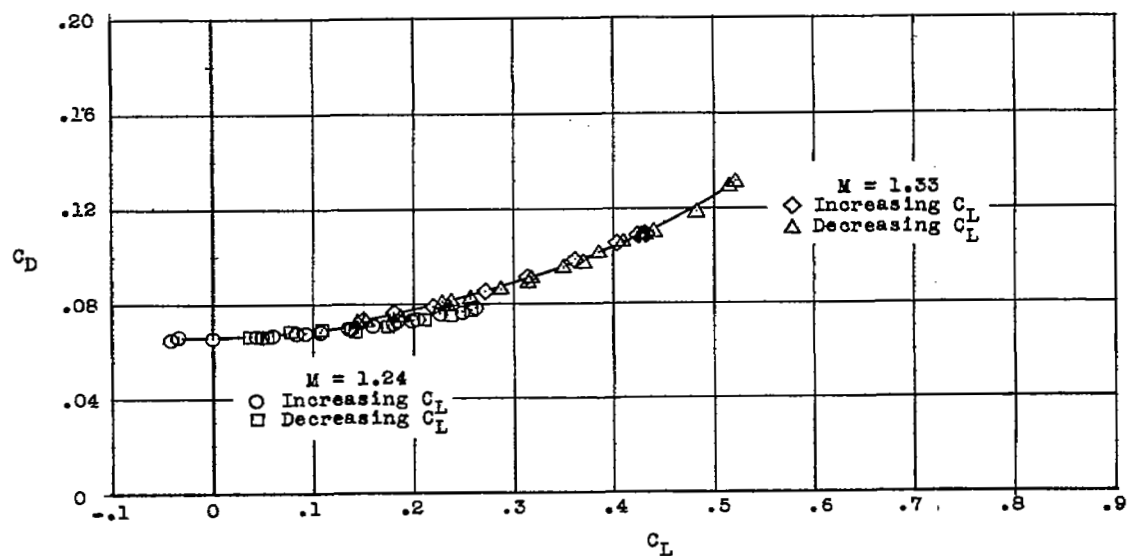


(b) Mach numbers 1.12 and 1.02.

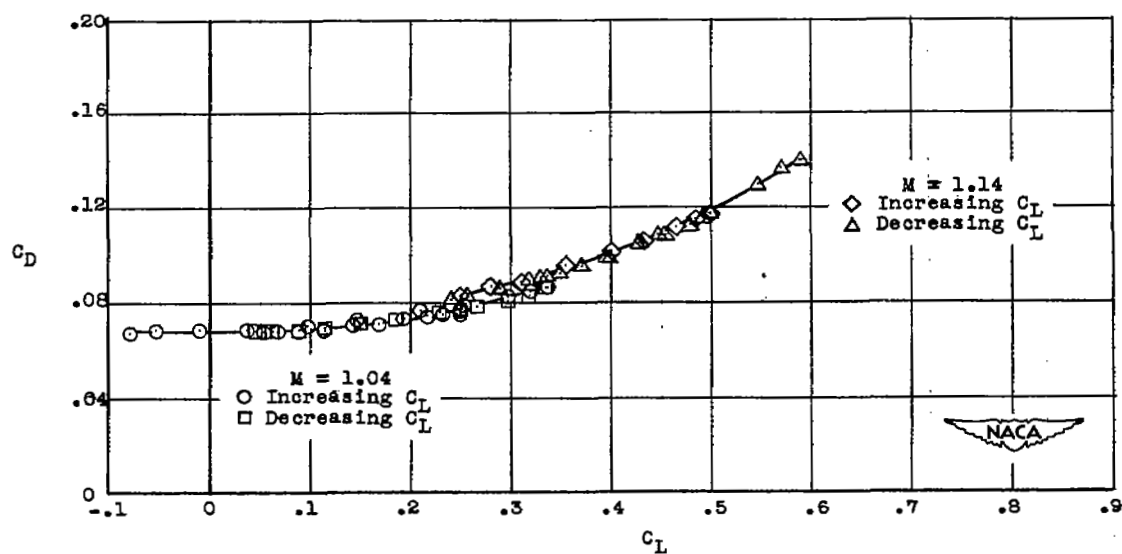


(c) Mach number 0.97.

Figure 20.- Steel-wing-model basic drag data.

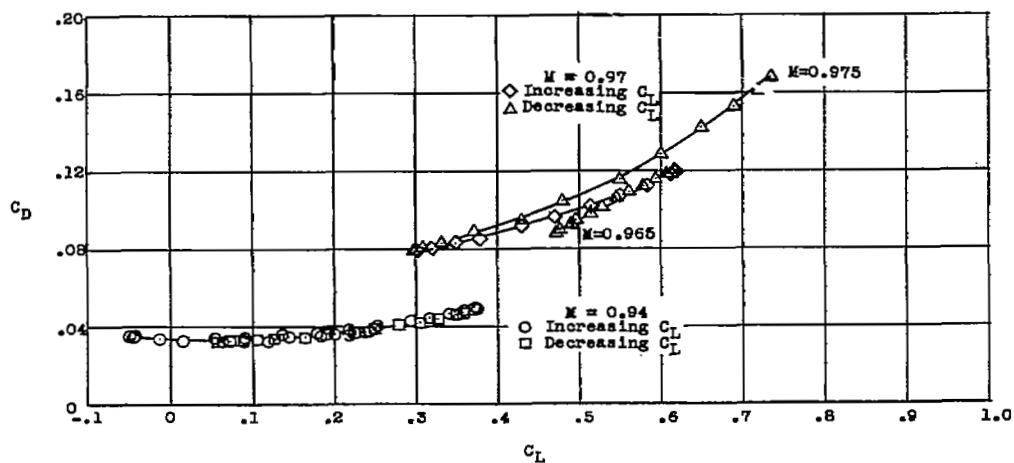


(a) Mach numbers 1.33 and 1.24.

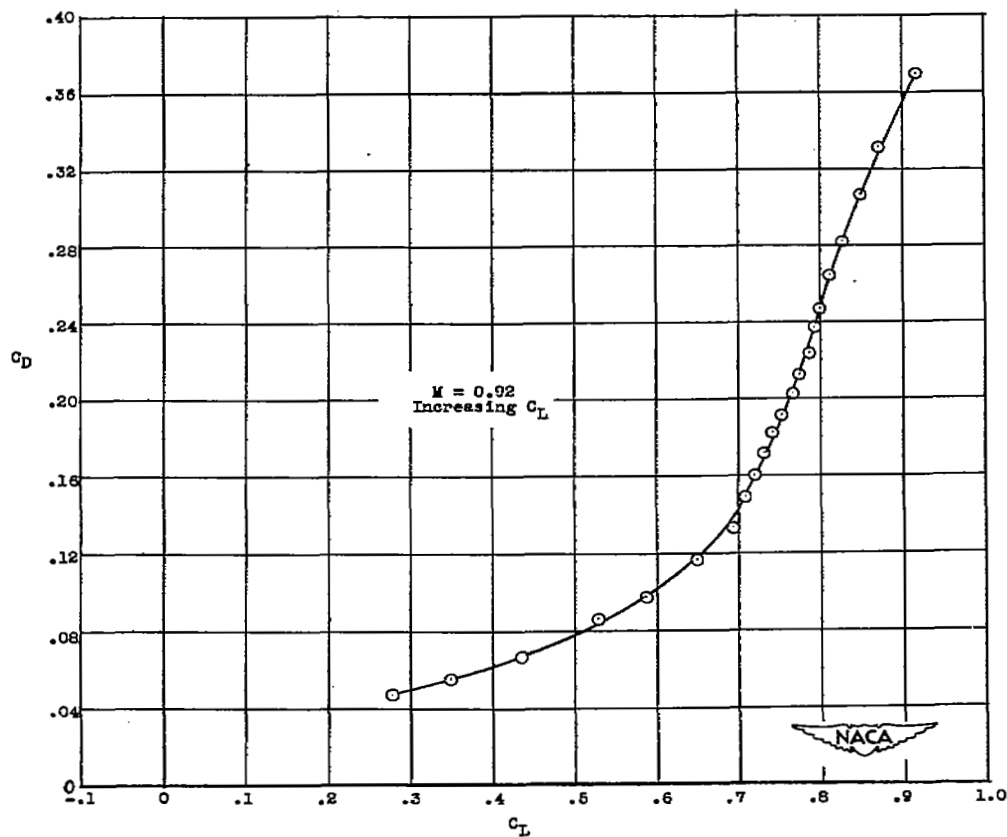


(b) Mach numbers 1.14 and 1.04.

Figure 21.- Duralumin-wing-model basic drag data.



(c) Mach numbers 0.97 and 0.94.



(d) Mach number 0.92.

Figure 21.- Concluded.

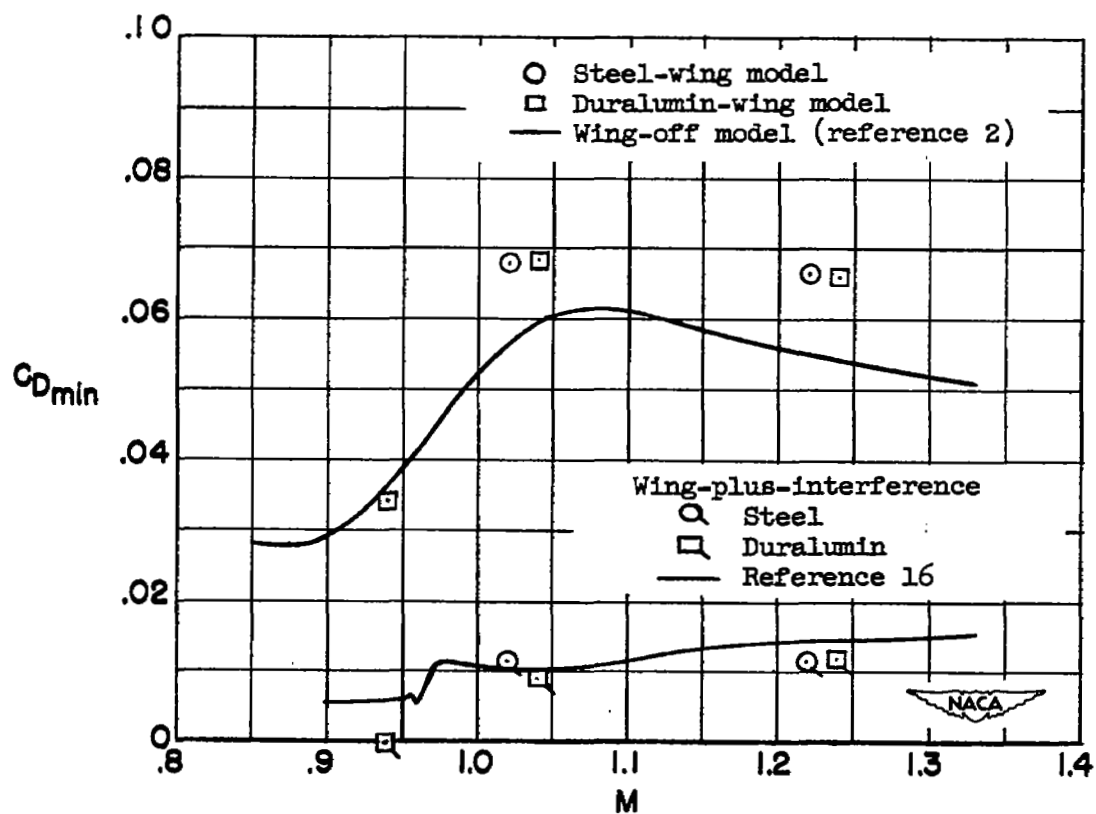


Figure 22.- Minimum drag coefficients.

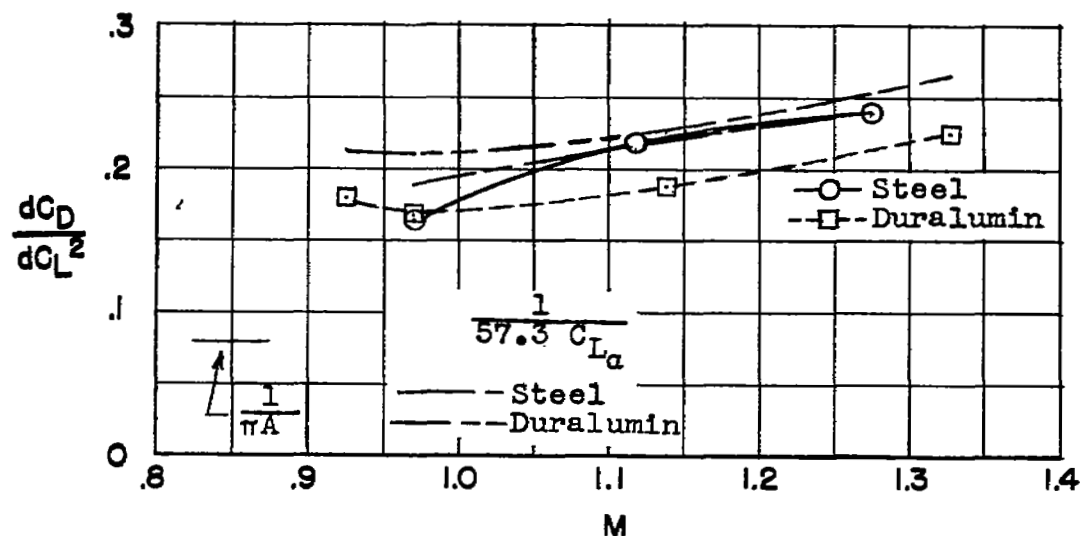
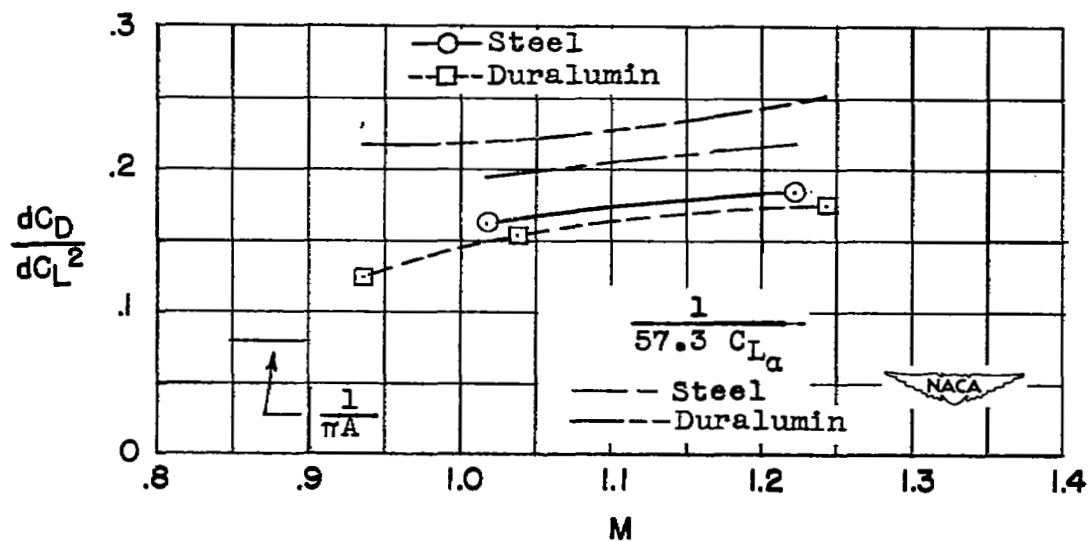
(a) $C_L \approx 0.50$.(b) $C_L \approx 0.15$.

Figure 23.- Effect of lift on drag.